Title
Trans-blood Imaging in the Heart using a Real-time Infrared Endoscopic System

Author
Low, Jason

Publication Date
2007

Peer reviewed|Thesis/dissertation

UNIVERSITY OF CALIFORNIA

Los Angeles

Trans-blood Imaging in the Heart using a Real-time Infrared Endoscopic System

A thesis submitted in partial satisfaction

of the requirements for the degree Master of Science

in Bioengineering

by

Jason Low

2017

ABSTRACT OF THE THESIS

Trans-blood Imaging in the Heart

using a Real-time Infrared Endoscopic System

by

Jason Low

Master of Science in Bioengineering

University of California, Los Angeles, 2017

Professor Warren Grundfest, Co-Chair

Professor Zachary Deis Taylor, Co-Chair

Intra-operative imaging during cardiac surgery remains insufficient for many applications. For example, intra-operative visualization of heart valves has not been standardized and current research techniques primarily utilize ultrasound, which exhibits poor contrast at the interface of blood and valve tissue. Sufficient resolution and contrast have been obtained with MRI, but the technique is slow and it is not currently practical nor routine to perform real-time MRI imaging for intraoperative use. Standard optical endoscopy has not translated because of the significant scattering and absorption of blood at the UV/VIS wavelengths. However, based on Mie optical scattering theory, imaging through blood using infrared light is theoretically feasible. In this project, we utilized components and technology from IR wavelengths (e.g. 1550 nm) to design a

rigid endoscope that optimized tradeoffs between absorption and scattering to achieve optical imaging in real-time through blood. The results of optical ray-tracing simulations demonstrated that a rigid endoscopic system that images through blood with 50 μm resolution is feasible.

The thesis of Jason Low is approved.

Daniel Ennis

Wentai Liu

Warren Grundfest, Committee Co-Chair

Zachary Deis Taylor, Committee Co-Chair

University of California, Los Angeles

2017

TABLE OF CONTENTS

CHAPTER 1: BACKGROUND OF HUMAN BIOLOGY 1
1.1 Anatomy and Physiology 1
1.1.1 The Heart 1
1.1.2 Heart Valves 2
1.2 Pathophysiology 4
1.2.1 Congenital Heart Valve Disease 4
1.3 Heart Valve Imaging Methods 5
1.3.1 Echocardiography 5
1.3.3 Radiography 7
1.3.4 Magnetic Resonance Imaging 8
1.3.5 Computed Tomography 9
1.4 Summary and Conclusions 10
CHAPTER 2: BACKGROUND OF OPTICAL THEORIES 11
2.1 Index of Refraction 11
2.2 Absorption 13
2.3 Scattering 15
2.4.1 Rayleigh Scattering 17
2.5.2 Mie Scattering 18
2.6 Summary and Conclusions 20
CHAPTER 3: IMAGING THROUGH BLOOD 21
3.1 Introduction 21
3.2 Absorption of Blood 22
3.3 Mie Scattering in Blood 24
3.4 Clinical Applications of Infrared Imaging 26
3.5 Summary and Conclusions 28
CHAPTER 4: INTRODUCTION TO ENDOSCOPE DESIGN 29
4.1 Introduction 29
4.2 Illumination System 31
4.2.1 Optical Fibers 31
4.2.2. Illumination Optics 33
4.3 Image Transmission System 36

4.3.1 Objective Lens 36
4.3.2 Conventional Relay 38
4.3.3 Gradient Index Lens Relay 40
4.4. Summary and Conclusions 42
CHAPTER 5: SIMULATIONS AND EXPERIMENTS 43
5.1 Introduction 43
5.2 Imaging System Design 45
5.2.1 Optical Lenses 45
5.2.2 Antireflective Coatings 46
5.2.3 Infrared Camera 49
5.3 Camera Evaluation 51
5.4 Sequential Ray-Tracing Simulations 54
5.4.1 System Setup 54
5.4.2 Lens Stock Matching Tool 54
5.4.3 Cross-sectional Layout 56
5.4.4 1st Order Optical Properties 56
5.4.5 Standard Spot Diagram 59
5.4.6 Transverse Ray Fan Plots 62
5.4.7 Field Curvature and Distortion 62
5.4.8 Wavefront Aberration Coefficients 63
5.4.9 Modulation Transfer Function 66
5.4.10 Image Simulation 66
5.4.11 Relative Illumination 68
5.4.12 Tolerance Analysis 68
5.5 Large Scale Objective Prototype 70
5.6 Illumination System Design 72
5.6.1 Infrared Illumination Source 72
5.6.2 Optical Fibers 72
5.7 Non-Sequential Ray Tracing Simulations 74
5.7.1 System Setup 74
5.7.2 Results and Discussion 76
5.8 Summary and Conclusions 79
CHAPTER 6: CONCLUSIONS AND FUTURE WORK 80
6.1 Summary of Work 80

6.2 Future Work and Experiments 81
6.2.1 Mechanical Design 81
6.2.2 In vitro experiments 82
6.2.3. In Vivo experiments 83
References 85

LIST OF FIGURES

Figure 1-1. Anatomy of the Heart ……...3

Figure 2-1. Snell's Law. ……12

Figure 2-2. Absorption of light by a chromophore……14

Figure 2-3. Light scattering due to a scattering particle……16

Figure 2-4. Rayleigh Scattering……17

Figure 2-5. Mie Scattering……19

Figure 3-1 Absorption spectrum of water, oxygenated and deoxygenated hemoglobin……...23

Figure 3-2. Scattering and Absorption plot of blood in logarithmic scale. ……...25

Figure 3-3. CardioOptics FIRE steerable fiber optic endoscope……...27

Figure 4-1. Example of a conventional rigid endoscope……...30

Figure 4-2. Total internal reflection inside an optical fiber……...33

Figure 4-3. Imaging optics at the distal end of an endoscope……35

Figure 4-4. Diagram of a retrofocus objective lens system……...37

Figure 4-5. Diagram of an example conventional relay system……39

Figure 4-6. Diagram of objective and the first stage of an example image relay system……..40

Figure 4-7. Example of GRIN rod lens. p is the pitch and r is the radius……..41

Figure 5-1. Block Diagram of Trans-Blood Imaging and Illumination System……...44

Figure 5-2. Shaded CAD models of two different imaging systems……46

Figure 5-3. Reflectivity of AR Coatings as a function of wavelength……..……48

Figure 5-4. Mechanical Dimensions of the QI-SCD15-M1 SWIR Camera……..……49

Figure 5-5. Specifications and spectral response for the QI-SCD15-M1 SWIR camera……...50

Figure 5-6. Fast Fourier Transform of Infrared Images…….……53

Figure 5-7. Lens prescription data for System 1 and System 2……..……..55

Figure 5-8. Cross-sectional layout of System 1 and System 2…….…….55

Figure 5-9. Standard spot-diagrams for three field positions……58

Figure 5-10. Transverse Ray Fan Plot for two different imaging systems……60

Figure 5-11. Field curvature and distortion plot for two different imaging systems…….61

Figure 5-12. Polychromatic modulation transfer function curves for two imaging systems…….64

Figure 5-13. Image simulation for two different imaging systems……65

Figure 5-14. Relative illumination curve for two different imaging systems ……..…….67

Figure 5-15. Large-scale Objective Prototype……..….71

Figure 5-16. Transmittance of Low OH Multimode Fiber as a function of wavelength. …….73

Figure 5-17. 3D Viewer of the illumination system on ASAP……..75

Figure 5-18. Simulated irradiance of the imaging system ……....76

Figure 6-1. CAD drawings of endoscope housing…..……...…….....82

Figure 6-2. Sample cuvette holder to be used in future *in vitro* experiments……..…..84

LIST OF TABLES

Table 2-1. Summary of Scattering Theories……..19

Table 5-1. AR Coating applied to each lens……..47

Table 5-2. 1st order optical properties for System 1 and System 2……...57

Table 5-3. Wavefront aberration coefficients for System 1 and System 2 ……...63

Table 5-4. Parameters used for Zemax tolerance analysis……..…69

Table 5-5. Bill of Materials for Large-Scale Objective Prototype…….70

Table 5-6. Low OH Multimode Fiber specifications ……73

.

CHAPTER 1:
BACKGROUND OF HUMAN BIOLOGY

1.1 Anatomy and Physiology

1.1.1 The Heart

The heart is a muscular organ in the cardiovascular system that continuously pumps blood to provide the body with vital oxygen and nutrients. A typical adult heart is approximately 12 cm x 8 cm x 6 cm and is divided into two separate pumps: the *right heart* (pulmonary circulation), which pumps deoxygenated blood to the lungs, and the *left heart* (systemic circulation), which pumps oxygenated blood from the lungs to the peripheral organs [1] [2]. Each of these pumps is composed of an upper chamber and a lower chamber: an *atrium*, and a *ventricle*. The atrium precedes the ventricle and is a weaker pump that moves blood into the ventricle. Thus, the walls of the atrium are thinner relative to the ventricles since relatively lower pressure is involved. The ventricles provide the main pumping force and pump blood through the pulmonary circulation via the right ventricle, or though the peripheral circulation via the left ventricle [3].

The *interatrial* septum and *interventricular septum* separate the two systems within the heart. The right heart is responsible for pumping deoxygenated blood originating from two large veins: the superior vena cava and the inferior cava. Deoxygenated blood enters the right atrium, passes through tricuspid valve into the right ventricle, and is pumped though the pulmonary valve into the pulmonary artery, which feeds into the lungs where the blood receives oxygen. The left heart is responsible for pumping the oxygenated blood coming into the heart from the pulmonary veins. Oxygenated blood enters the left atrium, passes though the mitral valve into the left ventricle, and is pumped though the aortic valve into the aorta for systemic circulation. The left ventricle is thicker and more muscular compared to the right ventricle since higher pressure is necessary to pump blood to the entire body. Figure 1-1 illustrates the anatomy of the heart and the direction of blood flow (Figure 1-1a) [1].

1.1.2 Heart Valves

Heart valves are structures inside the heart that allow blood to flow in one direction. They can be classified into two categories: the semilunar valves and the atrioventricular valves [2]. The semilunar valves consist of two valves: the aortic and the pulmonary artery valve. The purpose of these valves is to block the backflow of blood from the aorta and pulmonary arteries into the ventricles during diastole, which is part of the cardiac cycle when the ventricle is relaxed [5]. The opening and closing of the semilunar valves are done passively, which means that they close when a rapid pressure gradient pushes blood backwards [5]. Likewise, the valves open when a forward pressure gradient pushes blood in the forward direction. Similar to the semilunar valves, the atrioventricular valves (AV valves) also consist of two valves: the tricuspid valve and mitral valves. These valves block the flow of blood from the ventricles to the atria during systole,

which is the period of the cardiac cycle when the ventricles contract. Unlike the semilunar valves, the AV valves do not require backflow to close [5].

As seen in Figure 1-1b, papillary muscles are attached to the to the bottom of the AV valves by chord-like tendon structures called the chordae tendineae (Figure 1-1b) [1]. When the ventricular walls contract, the papillary muscles contract and pull the valves inward towards the ventricles. This prevents the valves from bulging too far backward in the direction of the atria during ventricular contraction. Problems can arise if the valves become dysfunctional, such as chorda tendineae rupture or if the papillary muscles become paralyzed, which would result in leaks that can lead to death of the patient [1]. The pathophysiology of valvular heart disease is discussed in more detail in the following section.

A **B**

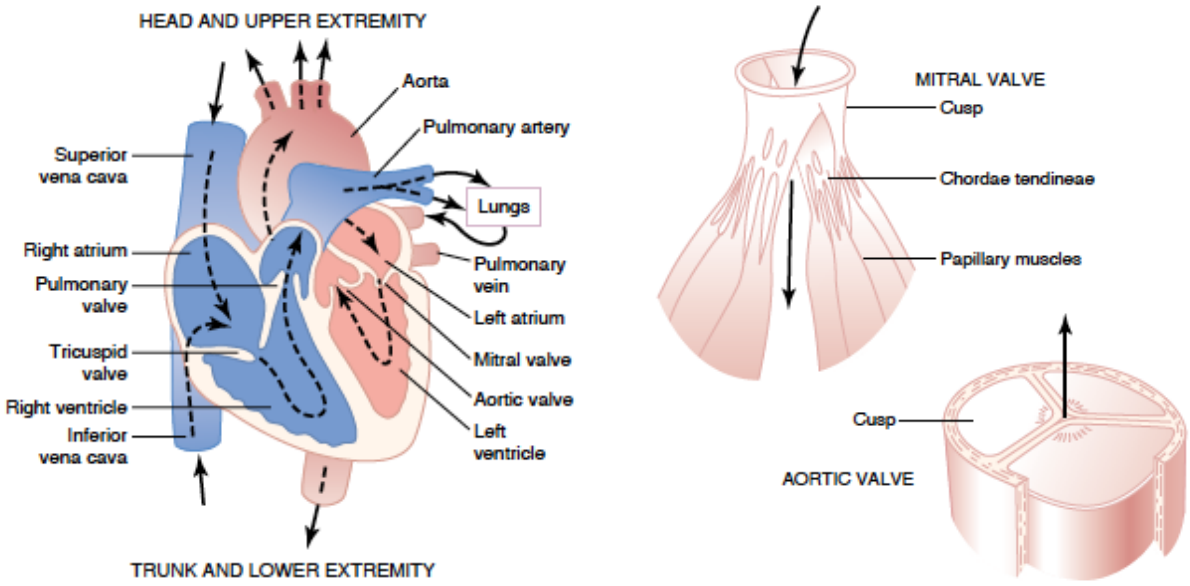

Figure 1-1 Anatomy of the Heart. A. The anatomy of the heart and the direction of blood flow through the heart chambers and heart valves. B. The left ventricular valves (mitral and aortic valves) [1].

1.2 Pathophysiology

Valvular heart disease affects over 4 million people and leads to more than 25,000 deaths annually in the United States [13]. Valvular heart disease refers to the dysfunction of any of the four heart valves described in the previous section. In general, there are two main forms of valvular heart disease: stenosis and regurgitation [6]. Stenosis is a condition where the heart valve becomes narrow due to thickening or calcification of the valve tissue. The other form of valvular heart disease is regurgitation, which is a condition where the dysfunctional valve allows blood to flow in the opposite direction. These valve problems can be either congenital, which means that the defect is present since birth, or acquired due to another cause in later in life [1]. Congenital heart valve disease is the motivation for this thesis and is discussed in more detail in the following section.

1.2.1 Congenital Heart Valve Disease

The most common type of heart valve defect is a congenital heart defect [7]. A congenital heart defect occurs in pediatric patients when the heart is incorrectly formed during fetal development. The most common cause of congenital heart defect is viral infection of the mother when the fetal heart is forming during the first trimester of pregnancy [1]. For example, an infection of the German measles virus can cause an expectant mother's baby to develop severe birth defects including heart defects. [9] [10]. However, not all congenital heart valve defects have a viral etiology.

Some congenital heart defects are hereditary. Children whose parents have received surgical treatment for congenital heart disease have a greater chance (ten times greater) of having a congenital heart disease compared to other children [1]. Additionally, the same heart defect that

has been known to occur in identical twins also occurs in the following generations. These defects are oftentimes associated with other congenital defects that are not limited to the heart. An example of a congenital heart valve condition is a bicuspid aortic valve, which is the result of fusing the two cusps during fetal development. A bicuspid aortic valve is the most common congenital heart anomaly, occurring in 4.6 out of 1000 births [8]. Oftentimes, patients with a bicuspid aortic valve will be asymptomatic, but if the valve leaflets do not close correctly, aortic regurgitation can occur. Bicuspid aortic valves can also become calcified, which could lead to aortic stenosis.

Other congenital heart valve defects include tricuspid atresia and pulmonary atresia. In tricuspid atresia, the tricuspid valve fails to develop which leads to the absence of a right ventricle. In pulmonary atresia, the pulmonary valve fails to develop which obstructs the flow of blood from the heart to the lungs. Treatment options for valvular heart disease include repairing the valve or replacing the valve with an artificial heart valve [1]. If the condition is left untreated, advanced heart valve disease can lead to heart failure, stroke, blood clots, or death. Therefore, early diagnosis of these conditions using imaging technologies is critical in improving patient outcomes.

1.3 Heart Valve Imaging Methods

1.3.1 Echocardiography

Echocardiography is the most common method to confirm the diagnosis of valvular heart disease using ultrasound [11]. Transthoracic echocardiography is a non-invasive process, which involves placing the ultrasound transducer on the patient's chest to view the internal structures of the heart. An advantage of echocardiography is that the resolution is <1cm. Besides imaging, a

useful feature of echocardiography that provides quantitative information is the ability to assess the direction and speed of blood flowing inside the heart via the Doppler effect [17]. For mitral valve stenosis, transthoracic echocardiography is used to show enlargements of the left atrium and calcified mitral valve [11]. For aortic and mitral regurgitation, reversal of blood flow using the Doppler feature can be observed [11].

However, echocardiography has several disadvantages. One disadvantage of ultrasound is that it is unable to differentiate between tissue types. To increase the resolution of the ultrasound image and differentiate between tissue types, higher frequencies (much greater than 2 MHZ) should be used for the ultrasound transducer [14]. Since higher frequencies have shorter penetration through tissue, the transducer must be located near the structure of interest to obtain a high-quality image. This is a limitation of transthoracic echocardiography because the ultrasound transducer is located externally on the patient's chest. Another disadvantage is that many factors can affect quality of the ultrasound image including the patient's size, air pockets, and bone. Additionally, imaging artifacts can occur due to the presence of air and the image quality is highly dependent on the skill of the ultrasound operator.

Intra-cardiac echocardiography is another ultrasound technique used to image structures and guide procedures inside the heart. Intra-cardiac echocardiography uses a minimally invasive catheter-based ultrasound transducer that is located at the tip of a catheter. The right atrium is the most commonly imaged structure of the heart with intra-cardiac echocardiography [15]. The ultrasound catheter is positioned into the right atrium under fluoroscopic guidance from the inferior vena cava via the femoral vein [18]. An alternative approach is to insert the catheter from the superior vena cava, via the right internal jugular vein or the left subclavian vein.

The main advantage of intra-cardiac echocardiography over transthoracic echocardiography is the ability to freely maneuver inside the heart. Intra-cardiac echocardiography also offers real-time visualization of cardiac structures and can be used intra-operatively [18]. However, a disadvantage is that the ultrasound physics for intra-cardiac echocardiography are the same as to transthoracic echocardiography, which means the resolution is dependent of the ultrasound frequency and the number of transducers. Also, macrostructures may be more difficult to image compared to transthoracic echocardiography due to the close distance of the intra-cardiac echocardiography catheter. Other limitations include difficulty recognizing cardiac structures due to distorted images, absorption of the ultrasound energy by the tissue, low signal to noise ratio, and catheter instability [16].

1.3.3 Radiography

Radiography, more commonly known as an X-ray, is an imaging method that provides information based on the density of chemical elements in tissues. Absorption of x-rays by the tissue is a result of ionizing the inner shell electrons of an atom. X-rays are often used to diagnose heart valve disease and in an application called fluoroscopy to guide cardiac procedures such as device implantation and radiofrequency ablation [13]. For diagnostic uses, a faint outline of the heart is produced in a standard chest radiograph, which may provide the physician with information regarding the general size of the heart. Based on the size of the heart, a physician can determine whether the patient may have hypertrophy related to heart valve disease. Specifically, a chest x-ray showing enlargement of the left atrial could suggest mitral stenosis [11]. Additionally, a radiograph showing a calcific aortic valve and enlarged left ventricle and atrium could suggest aortic valve stenosis [11].

A disadvantage of radiography is that the method involves exposing the patient to damaging ionizing radiation in the form of x-rays, which requires the risks to be balanced with the benefits of the procedure [12]. Another limitation of radiography is that it has been shown to underestimate the severity of stenosis because it cannot be used to image surface features. Therefore, radiography is often used in conjunction with other imaging methods, such as ultrasound, in the diagnosis of heat valve disease [13].

1.3.4 Magnetic Resonance Imaging

Magnetic Resonance Imaging (MRI) is a non-invasive imaging technique used to visualize the structure and function of the heart in patients with congenital heart valve disease. Cardiac MRI is generally used in conjunction with the previously described imaging methods, if those methods fail to provide the physician with sufficient diagnostic information. Specifically, cardiac MRI can be used to quantify the degree of myocardial hypertrophy, ventricular dilation, and ventricular function as well as identify and quantify the degree of stenosis or regurgitation.

The procedure for cardiac MRI is similar to that of traditional MRI. The patient is placed into a loud narrow tube, where powerful magnets are used to align and excite the spin axis of hydrogen protons in the water molecules of the tissues being imaged. Radiofrequency signals emitted by the excited hydrogen protons are detected by a receiver and are used to generate images of inside the body. To avoid imaging artifacts due to motion of the heart for cardiac MRI, imaging data is only acquired during specific portions of the cardiac cycle, using a process called ECG gating. Although real-time MRI technology is emerging in the interventional suite for cardiological applications, it is currently impractical for intraoperative use.

An advantage of cardiac MRI is that it provides greater contrast for soft tissues compared to other imaging methods and does not expose the patient to ionizing radiation. Unlike echocardiography, MRI is not affected by imaging artifacts due to bone or air. However, MRI also has several disadvantages. The disadvantages of MRI are that it is time-consuming, expensive and may not be widely available in clinics. MRI may also be difficult for patients with claustrophobia and is contraindicated for patients with metallic implants such as cardiac pacemakers or defibrillators.

1.3.5 Computed Tomography

Another non-invasive cardiac imaging method used to evaluate heart valve disease is computed tomography (CT). In cardiac CT, the patient is first injected with an iodine-based intravenous contrast agent. After the contrast agent is injected, multiple cross-sectional x-ray images of the patient are taken from different angles and combined to produce a high-resolution three-dimensional image. Cardiac CT is generally used in conjunction with other imaging methods if those methods fail to provide sufficient diagnostic information. For example, CT may be used after echocardiography to identify and better assess the structure and function of valves when vegetation due to bacterial endocarditis is suspected. Patients with congenital heart disease may also undergo cardiac CT with echocardiography to carefully monitor changes after surgical treatment.

The advantage of CT over other cardiac imaging methods is that multi-slice scanners can be used to obtain high temporal and spatial resolution without motion artifacts. In addition, compared to MRI, it is not contraindicated for patients with metallic implants. However, the disadvantage of CT is that it exposes the patient to high doses of ionizing radiation, which limits

its use for children and pregnant women. Additionally, because the contrast agent is iodine-based, CT may be contraindicated for patients with hyperthyroidism and who are allergic to iodine.

1.4 Summary and Conclusions

Despite the advantages that current cardiac imaging methods offer, the ideal method for visualizing the structures of heart valves inside the heart is optical imaging [21]. Unlike ultrasound images, optical images are less distorted because light scatters off surfaces instead of being absorbed by the tissue [14]. Additionally, it is theoretically possible to obtain higher resolution images in optical systems, which may offer greater power in detecting physical abnormalities in the early stages before they become visible under x-ray or ultrasound. Another advantage of optical imaging is the ability to be used intra-operatively, as opposed to other medical imaging modalities such as traditional MRI and CT. Therefore, the ability to optically image structures inside the heart should be investigated and thus is the motivation of this thesis. The related theories for optical imaging inside the heart through blood are discussed in the following chapters.

CHAPTER 2:
BACKGROUND OF OPTICAL THEORIES

2.1 Index of Refraction

The index of refraction, n, is an optical property that describes how light propagates through a medium. It is defined as the ratio of the speed of light in a vacuum to the speed of light in the medium [19]. Since the speed of light is always greater in a vacuum than it is in a medium, n is always greater than 1. Snell's law calculates how light behaves when it passes through a boundary of two different media:

$$n_1 \sin \theta_1 = n_2 \sin \theta_2 , \qquad \text{(Eq. 2-1)}$$

where n_1 is the index of refraction of the first medium, n_2 is the index of refraction of the second medium, θ_1 is the angle of incidence, and θ_2 is the angle of refraction (Figure 2-1). According to Snell's Law, when $n_2 > n_1$, the light bends towards the normal; when $n_1 > n_2$, the light bends away from the normal.

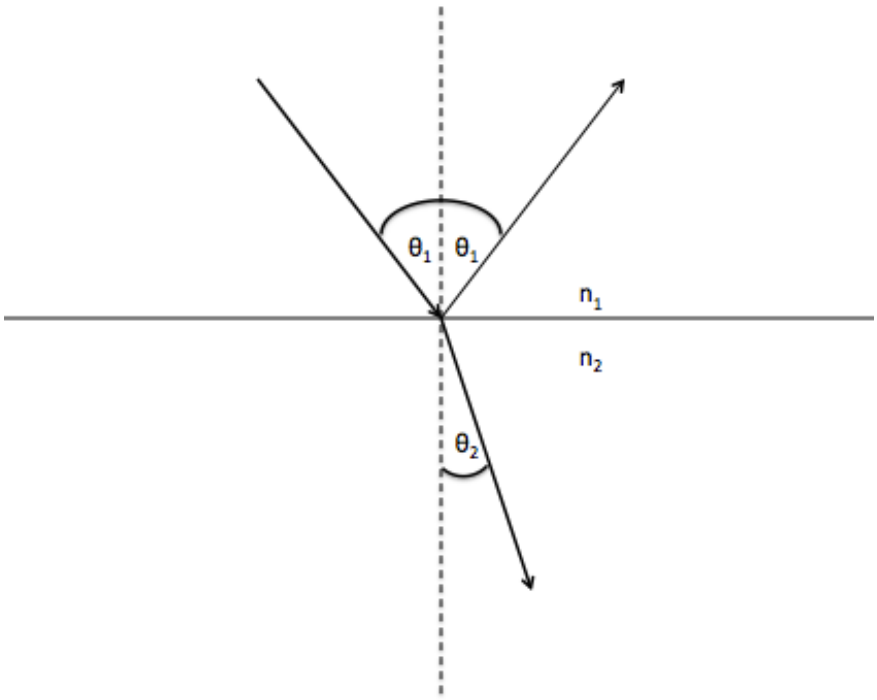

Figure 2-1. Snell's Law. Refraction of light at the interface between two different media. The refractive index mismatch results in a partial reflection of the incident light called Fresnel reflection [20].

2.2 Absorption

Absorption is the process in which the energy of incident light is taken up by a chromophore (Figure 2-2). A chromophore is the part of a molecule that absorbs or reflects light. Depending on the chromophore, light can be absorbed via electronic transitions or vibrational transitions. Electronic transitions are associated with the absorption of wavelengths in the ultraviolet, visible and near-infrared regions of the electromagnetic spectrum. A few examples of biological chromophores that that undergo electronic transitions include hemoglobin, vitamin b12, and cytochrome C. Specifically, hemoglobin strongly absorbs in the red-near infrared region of the electromagnetic spectrum. Vibrational transitions are generally associated with the infrared region of the electromagnetic spectrum. Water is the main chromophore in biological systems that absorbs via vibrational transitions [22].

Absorption is characterized by the absorption cross-section and the absorption coefficient. The absorption cross section, σ_p, which represents the probability of an absorption process, is calculated by the following equation [23]:

$$\sigma_a = P_a / I_0 \ , \qquad \text{(Eq. 2-2)}$$

where P_a is the power of the absorbed light, and I_0 is the intensity of the incident light.

The absorption coefficient, μ_a, which represents the cross-sectional area per unit volume, is calculated by the following equation [23]:

$$\mu_a = \rho_a \times \sigma_a \ , \qquad \text{(Eq. 2-3)}$$

where ρ_a is the volume density of absorbing particles and σ_a is the absorption cross section defined above. The absorption coefficient is in units per length.

From the absorption coefficient, the absorption mean free path, l_a, can be calculated by the following equation [23]:

$$l_a = 1/\mu_a \,, \qquad \text{(Eq. 2-4)}$$

where μ_a is the scattering coefficient derived above. The absorption mean free path is the average distance that light travels before interacting with the next absorbing particle.

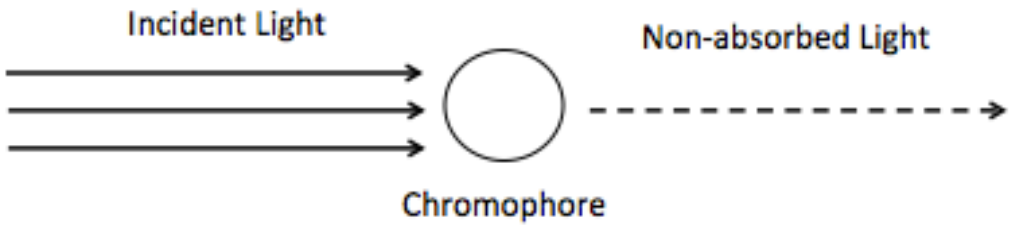

Figure 2-2. Absorption of light by a chromophore.

2.3 Scattering

Scattering is the process where light is forced to deviate from its straight trajectory due to local non-uniformities in the medium (Figure 2-3). It can be classified based on whether kinetic energy is transferred [22]. In inelastic scattering, the kinetic energy of the light after interacting with the scattering particle either increases or decreases. However, in elastic scattering, the kinetic energy of the light after interacting with a scattering sphere is unchanged. Depending on the size of the scattering particle relative to the wavelength of incident light, the theory of elastic scattering is described by two different theories: Rayleigh Scattering and Mie Scattering (Table 2-1).

Similar to absorption, scattering is characterized by the scattering cross section and the scattering coefficient. The scattering cross section, σ_s, which represents the size of the scattering shadow in units of area, is larger than the geometrical cross section. It is calculated by the following equation [23]:

$$\sigma_s = P_s / I_0 \ , \qquad \text{(Eq. 2-5)}$$

where P_s is the power of the scattered light, and I_0 is the intensity of the incident. The scattering coefficient, μ_s, which represents the cross-sectional area per unit volume, is calculated by the following equation [23]:

$$\mu_s = \rho_s \times \sigma_s \ , \qquad \text{(Eq. 2-6)}$$

where ρ_s is the volume density of scattering particles and σ_s is the scattering cross section defined above. The scattering coefficient is in units per length. From the scattering coefficient, the scattering mean free path, l_s, can be calculated by the following equation [23]:

$$l_s = 1/\mu_s \ , \qquad \text{(Eq. 2-7)}$$

where μ is the scattering coefficient derived earlier. The mean free path is the average distance that light travels before interacting with the next scattering particle.

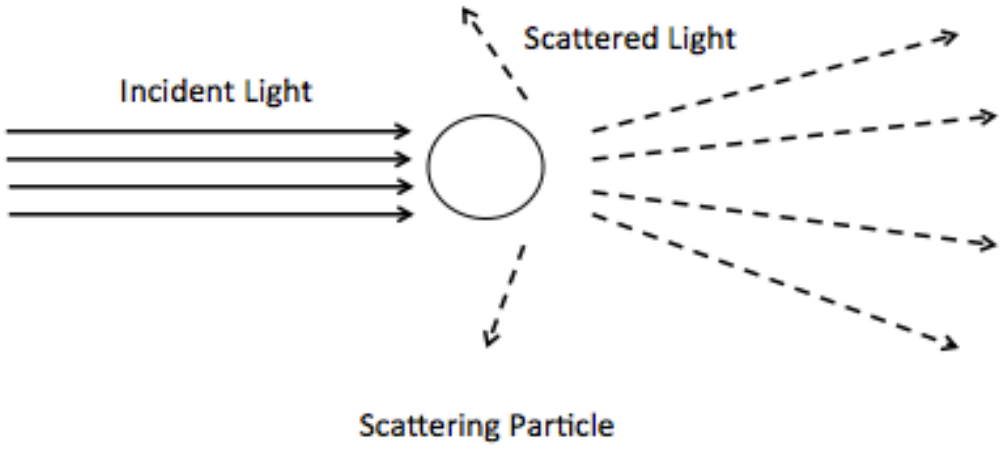

Figure 2-3. Light scattering due to a scattering particle.

2.4.1 Rayleigh Scattering

Rayleigh Scattering theory describes the effect of light scattering when the scattering particles are much smaller than the wavelength of light. When a uniform electric field from the incident light interacts with the scattering particle, a dipole moment is created [24]. Dipole radiation resulting from the dipole moment is given off in all directions at the same frequency as the incident light (Figure 2-4). The intensity of light scattered from a single particle, *I*, can be calculated from the following equation [25]:

$$I = I_0 \left(\frac{1 + \cos^2 \theta}{2R^2} \right) \left(\frac{2\pi}{\lambda} \right)^4 \left(\frac{n^2 - 1}{n^2 + 2} \right)^2 \left(\frac{d}{2} \right)^6, \qquad \text{(Eq. 2-8)}$$

where I_0 is the intensity of the incident light, θ is the scattering angle, n is the index of refraction of the particle, λ is the wavelength of incident light, d is the diameter of the scattering particle, and R is the distance to the particle from the observer. According to this equation, the intensity of light scattered is proportional to the fourth power of the inverse of the wavelength.

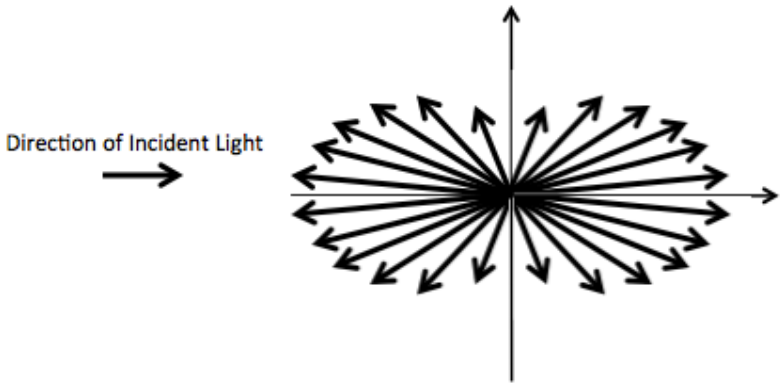

Figure 2-4. Rayleigh Scattering. The distribution of the scattered light intensity is in all directions.

2.5.2 Mie Scattering

Mie Scattering theory describes the effect of light scattering without considering the limitations resulting from the size of the scattering particle or wavelength of light. Unlike Rayleigh scattering theory, where $r \ll \lambda$, this type of scattering is important when the size of the scattering particle is similar to the wavelength of light. The direction of scattered light is in the forward direction of the incident light, as opposed to all directions (Figure 2-5) [26]. Mie theory has been previously applied in military and space sciences to see though particulate suspensions such as fog, mist and space dust. For example, using infrared cameras in satellites allows for greater ground penetration though haze compared to visible cameras. In astronomy, infrared telescopes are used to image father distances compared to visible telescopes because they can see though space dust.

The anomalous diffraction approximation quantifies Mie Scattering by calculating the extinction efficiency Q. The extinction efficiency is defined as the ratio of the scattering cross section and the physical cross section [27]:

$$Q = 2 - \frac{4}{p}\sin p + \frac{4}{p^2}(1 - \cos p), \qquad \text{(Eq. 2-9)}$$

where p is the phase delay of the light wave interacting with the center of the sphere. The phase delay is calculated by the following equation [27]:

$$p = 4\pi a(n-1)/\lambda\ , \qquad \text{(Eq. 2-10)}$$

where a is the radius of the sphere, n is the ratio of the refractive index of the media to the refractive index of the particle, and λ is the wavelength of the light. According to this equation, the scattering cross section is dependent on the second power of the inverse of the wavelength.

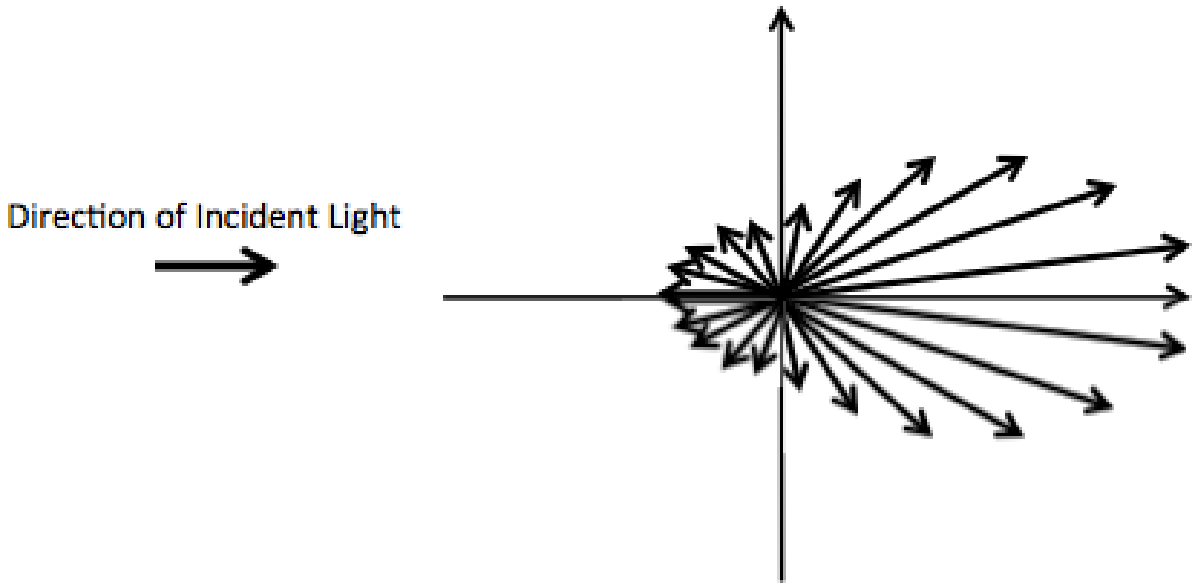

Figure 2-5. Mie Scattering. The distribution of the scattered light intensity is mainly in the forward direction of the incident light.

Table 2-1. Summary of Scattering Theories

Scattering Theory	**Size of Scattering Particle**	**Dependence on Wavelength**
Rayleigh Scattering	$r << \lambda$	$1/\lambda^4$
Mie Scattering	$r \sim \lambda$	$1/\lambda^2$
Reflective Scattering	$r >> \lambda$	Independent of λ

2.6 Summary and Conclusions

The purpose of this chapter was to introduce basic optical theory in context of imaging through blood. Several physical phenomena occur when light interacts with human tissue such as blood. Specifically, light can behave by reflecting, absorbing, transmitting, or scattering. The emphasis of this thesis is on scattering phenomenon, which is the process when light is changed due to local non-uniformities. There are two different scattering theories that depend on the wavelength and the size of the scattering particle. Rayleigh scattering theory applies when the size of the scattering particle is much smaller than the wavelength of light, while Mie scattering is valid when the size of the scattering particle is approximately the size of the wavelength. In the next chapter, Mie scattering will be discussed in more detail in the context of imaging though blood.

CHAPTER 3:
IMAGING THROUGH BLOOD

3.1 Introduction

Blood can be modeled as a particulate suspension, a heterogeneous mixture of suspended red blood cells dispersed in plasma. If left undisturbed, blood will separate into its component phases: 45% by volume of red blood cells and 55% by volume of plasma [31]. Plasma is mainly composed of water (90% water and 10% proteins), while red blood cells are approximately 7 μm in diameter, bi-concave shaped disks composed of hemoglobin solution [31]. At visible wavelengths, water is transparent but blood is opaque because of absorption by hemoglobin and scattering of red blood cells. The refracted transmitted light that enters blood either becomes scattered or absorbed. The percent transmission of visible light though blood can be calculated by the following equation [32]:

$$T_{visible} = \exp((-\alpha_h+\sigma) \times l) \qquad \text{(Eq. 3-1)}$$

where l is the path length through blood, α_h is the extinction coefficient due to absorption, and σ is the extinction coefficient due to scattering. This equation calculates the magnitude of visible light attenuation through blood by disregarding the absorption of water.

3.2 Absorption of Blood

As seen in the absorption spectrum of hemoglobin, significant absorption occurs in the visible region of the electromagnetic spectrum (Figure 3-2) [31]. This partially explains why it is difficult to see through blood with visible light. When the wavelength increases to the infrared region, imaging through blood becomes feasible from the perspective of hemoglobin due to the decrease in the absorption coefficient. As seen in the absorption spectrum of pure water, water is transparent in the visible region (Figure 3-1) [31]. However, as the wavelength increases to the infrared region, absorption of water also increases in bands, with many local minima and maxima. The maxima correspond to wavelengths where the chromophore is more absorptive while the minima correspond to wavelengths where the chromophore is least absorptive. The source of these bands is due to the stretching, bending and rotating resonance frequencies of water. Since blood is composed of mainly water, the shape, including maxima and minima, of the absorption curve of water is very similar to that of blood. However, the absorption coefficient of blood would be less than that of pure water, since impurities such as proteins and lipids disturb the resonant motion of the water molecules.

In the infrared region, the absorption of water must be accounted for. Therefore, the equation derived previously (Eq. 3-1) needs to be modified to include the absorption of water for

the infrared wavelengths. The equation can be rewritten with the absorptions terms weighed according to the composition of blood (45% hematocrit and 65% water) [32]:

$$I_{infrared} = \exp\left(-\left(0.45\,\alpha_h + 0.65\alpha_{water} + \sigma\right) \times l\right) \qquad \text{(Eq. 3-2)}$$

where l is the path length through blood, α_h is the extinction coefficient due to absorption of hemoglobin, α_{water} is the extinction coefficient due to absorption of water, and σ is the extinction coefficient due to scattering.

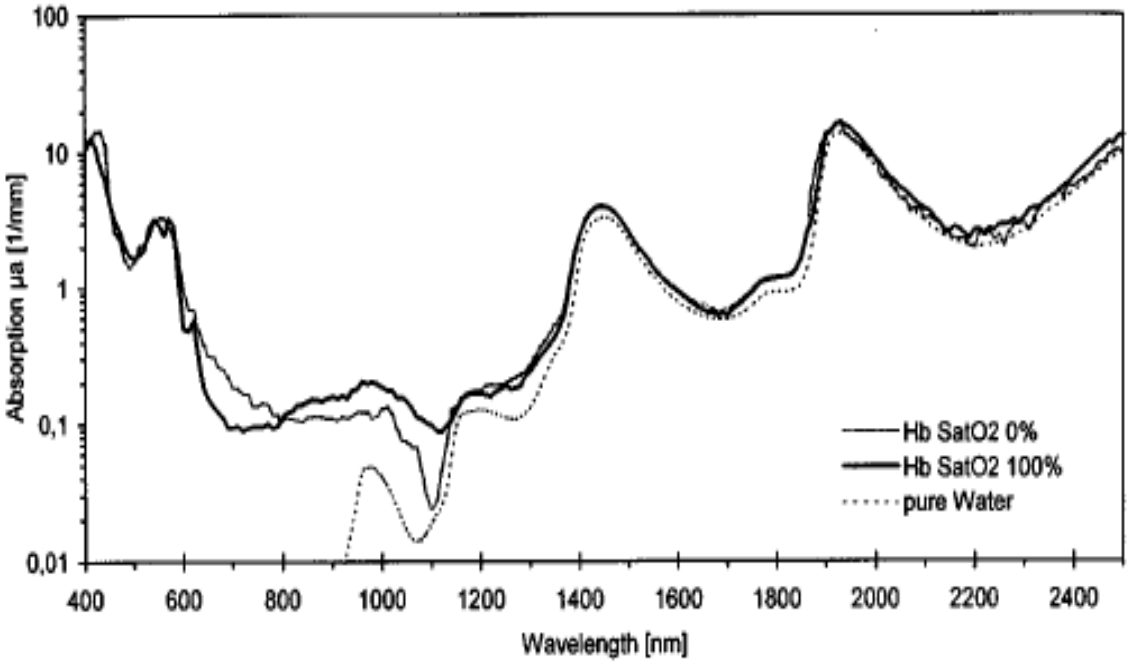

Figure 3-1 Absorption spectrum of pure water, oxygenated and deoxygenated hemoglobin [31].

3.3 Mie Scattering in Blood

For imaging though blood, scattering is more difficult to overcome compared to absorption. This is because the method to overcome absorption, which is increasing the intensity of the illumination, does not apply for scattering. Instead, Mie Scattering theory is used to overcome the effect of scattering when imaging though blood. According to Mie theory, visualization through blood can be achieved with infrared wavelengths, which are long enough to see past the scattering particles (red blood cells). The minimum wavelength can be calculated by the following equation [30]:

$$\lambda_C = 3\ d\ \Delta n \qquad \text{(Eq. 3-3)}$$

where λ_C is the critical wavelength, d is the effective spherical diameter of the red blood cell, and Δn is the difference in refractive indices between red blood cells and plasma. The refractive index of red blood cells is greater than that of plasma. Solving the above equation (Eq. 3-3) with the following values: d= 5.5μm Δn= 0.06, λ_C = 990nm.

Previous studies found in literature have shown the using shorter near-infrared wavelengths of ~990nm have been unsuccessful because it resulted in significant scattering [30]. This is because the equation used above from Mie theory is an approximation that makes several assumptions. The first assumption is that Mie theory makes it that red blood cells are modeled as spherical particles with an effective diameter of 5.5 um, even though they are bi-concave disks. Another assumption is that the red blood cells are separated at a distance much greater than the wavelength of light. This assumption is necessary to avoid the case of multiple scattering, which requires extremely complex equations to solve and are beyond the scope of this thesis.

For experimental verification, Grundfest et al. successfully used illumination between 1550 and 1650 nm, which decreased the amount of scattering but increased the effect of water absorption compared to the near infrared wavelengths [30]. Although the absorption is greater at higher wavelengths, it can be overcome by increasing the intensity of illumination. Figure 3-2 illustrates difference in scattering and absorption in the region of 1000 to 1300 nm (Region 1) and 1500 to 1900 nm (Region 2). The second region was preferred over the first region since the scattering effect is less while the effect of absorption was only slightly greater.

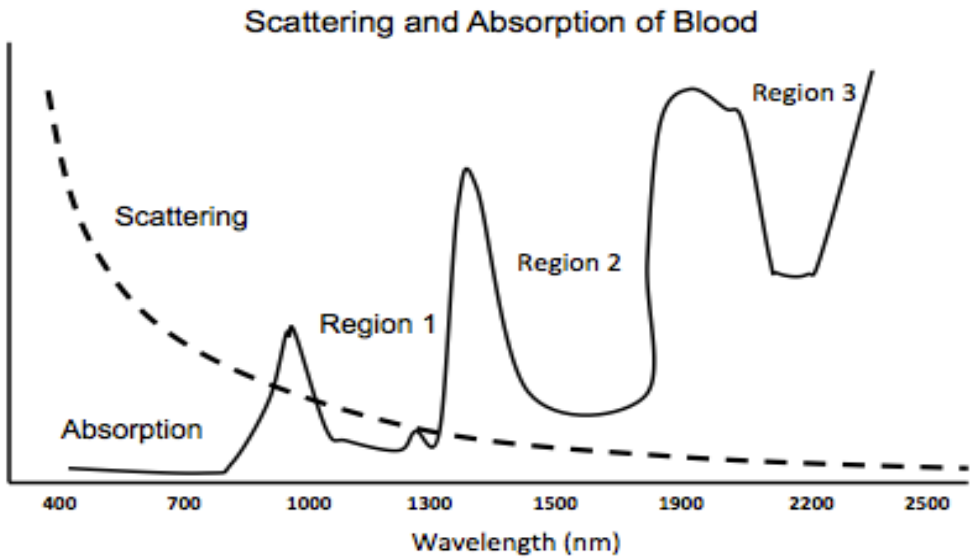

Figure 3-2. Scattering and Absorption plot of blood in logarithmic scale. The solid line indicates the absorption plot of blood and the dashed line indicates the scattering plot of blood. *(Adapted from Grundfest et al.* [30]).

3.4 Clinical Applications of Infrared Imaging

A trans-blood endoscopic imaging system would have numerous clinical applications in cardiology. Applications include observing malformed structures, navigating catheters, making diagnoses and performing surgical procedures in the heart. For example, an important distinction that a physician can make using infrared imaging is to diagnose whether a heart valve defect is structural or vegetative. Infrared imaging can also be used to assist in surgical procedures such as suturing, excising, and stapling without needing to perform open-heart surgery. Besides diagnosing and repairing heart valve defects, trans-blood imaging would be useful for thoroughly assessing the location of septal defects, myocardial infarctions, as well as the nature of heart or artery transpositions before surgery. Trans-blood imaging would also be useful after the treatment of heart valve disease. For example, artificial heart valves can be inspected for blood clots or structural damage and replaced before failures occur [21].

Several animal and clinical studies were conducted using the Cardio Optics Cardiac Optical Imaging System (Cardio Optics, Boulder CO), the first commercially available infrared endoscopic system approved for trans-blood imaging (Figure 3-3). The flexible fiber-optic catheter system received 510(k) approval by the Food and Drug Administration in 2006, specifically for the "visualization of the cardiac chambers and great vessels" [35]. A study conducted by Nazarian et al. assessed the feasibility of directly visualizing the coronary sinus ostium using the Cardio Optics system. The authors concluded that direct visualization of the coronary sinus ostium would help facilitate lead and catheter placement [33]. In a study conducted by Knight et al. using the same system, it was determined that imaging of intra-cardiac structures and the electrode-tissue interface was feasible during radiofrequency catheter ablation, which could result in more precise and shorter RF ablation procedures [34].

Additionally, Grundfest et al. demonstrated that it was possible to image the coronary sinus, tricuspid valve, and great vessels in various animal models. After obtaining FDA 510(k) approval, Grundfest et al. demonstrated successful visualization in the heart during placement of electrophysiological leads via right heart catheterization [30].

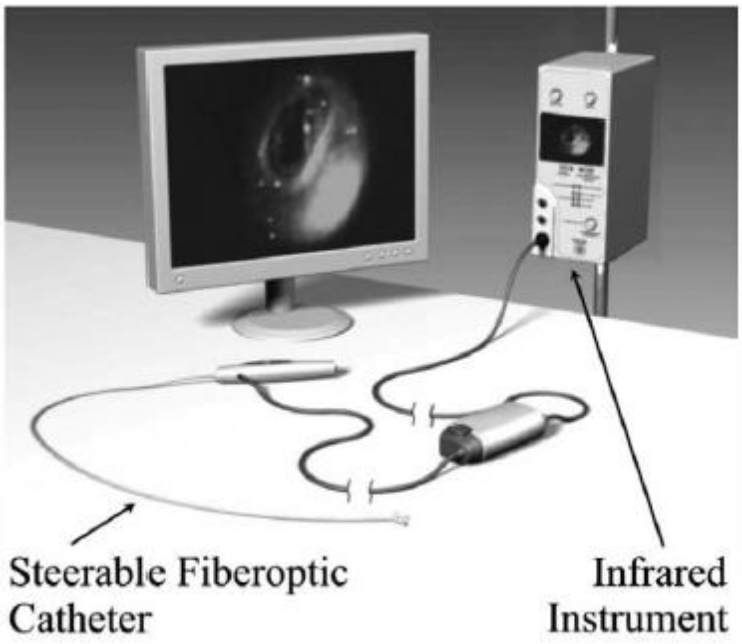

Figure 3-3. CardioOptics FIRE steerable fiber optic endoscope system [33].

3.5 Summary and Conclusions

This chapter introduced the optical properties of blood with an emphasis on absorption and scattering. Blood is modeled as a particulate suspension, a heterogeneous mixture of suspended red blood cells dispersed in plasma. A significant amount of absorption in blood occurs in the visible region of the electromagnetic spectrum due to the presence of hemoglobin, which prevents the use of imaging with visible light. According to Mie theory, visualization through blood can be achieved with infrared wavelengths, which are long enough to see past the scattering particles. An infrared fiber optic endoscope developed by Cardio Optics was the first infrared endoscopy system approved for trans-blood imaging based on Mie Scattering Theory. Multiple studies were performed on this imaging system to evaluate its potential applications. In the next chapter, endoscope design detailing illumination and image transmission will be discussed.

CHAPTER 4:
INTRODUCTION TO ENDOSCOPE DESIGN

4.1 Introduction

Endoscopes are medical devices that enable physicians to image tissues and organs inside the human body that would otherwise be inaccessible. The images are used intra-operatively to guide surgical procedures or to diagnose diseases. Depending on the area of the body that needs to be imaged, the endoscope can be flexible or rigid. In a rigid endoscope, a rigid tube houses all the optical lens components of the system. However, in a flexible endoscope, a fiber optic cable relays imaging data from a miniature camera located at the distal tip of the endoscope. Regardless, both types of endoscopes work by first illuminating a target and then relaying an image of the target to a detector. There are five basic components of an endoscope: the illumination system, the imaging system, the image transmission system (relay system), and the viewing system. The basic principles of these components in a conventional rigid endoscope are introduced in this section.

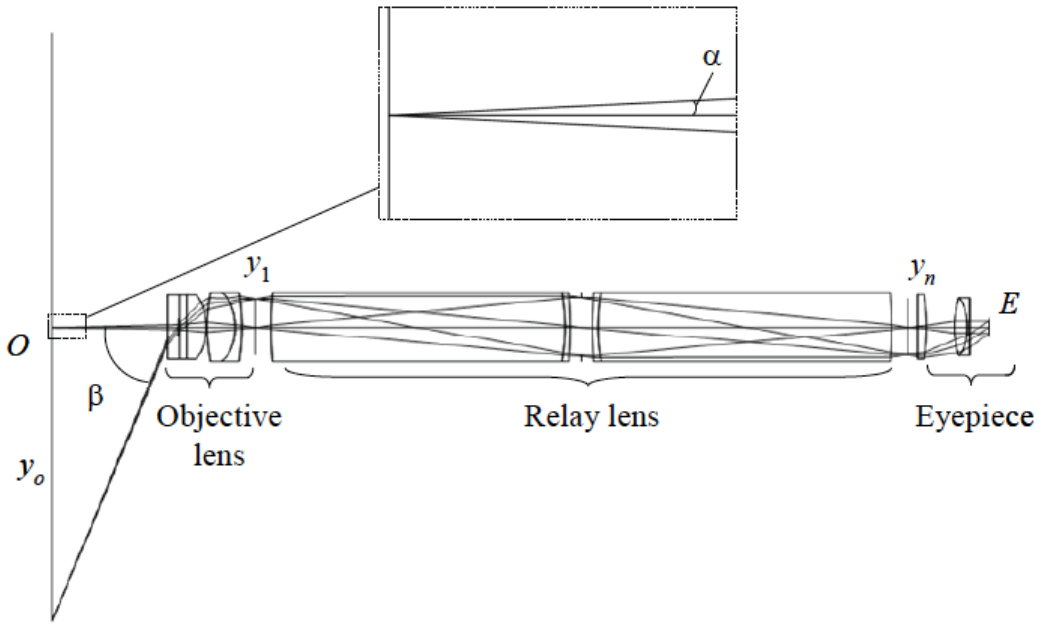

Figure 4-1. Example of a conventional rigid endoscope consisting of the objective lens, relay lens, and eyepiece, where y_0 is the height of the imaging field, y_1 is the height of the first image, y_n is the height of the final image though the relay system, and E is the exit pupil of the eyepiece [36]

Figure 4-1 is a diagram of a conventional rigid endoscope without the illumination system (Figure 4-1). The first component located at the distal end is the objective lens, which is part of the imaging system that creates y_1, an inverted image of y_0. The second component is the relay lens system, which relays the first intermediate image, y_1, through a series of multiple relay lenses to generate the final image, y_n at the opposite end of the endoscope. The final component located at the proximal end is the eyepiece or focusing lens, which are part of the viewing system. The purpose of the eyepiece or focusing lens is to focus the image to the eye or an electronic imaging sensor. An eyepiece is commonly found on older endoscopes, which produces a magnified virtual image for the observer. Instead of an eyepiece, newer endoscopes have a focusing lens, which is similar to a camera lens that produces a real image on an electronic

imaging sensor. After the sensor captures image, the electronic signal is relayed down a camera cable to an image-processing unit. The image-processing unit is connected to a CPU, which transmits the signals to the video processor so an observer can view the image on a monitor or display in real-time.

4.2 Illumination System

The purpose of the illumination system is to introduce uniform light to the imaging field. The requirements of an endoscopic illumination system include: sufficient light intensity, uniform illumination, high coupling efficiency, and large field of view. Sufficient light intensity is difficult to achieve in endoscopes with small diameters due to the lack of space to transmit the light. At the same time, light intensity is also limited by the possibility of blood or tissue damage. Low light collection efficiency is an issue due to the size of the aperture. These factors also depend on the light source, transmission, and illumination method.

4.2.1 Optical Fibers

In fiber illumination, an incoherent fiber bundle consisting of tens of thousands of individual fibers transmits light from the light source to the region of interest at the distal end of the endoscope. Each fiber directs the light with minimal losses via total internal reflection. For total internal reflection to occur, the refractive index of the fiber core has to be greater than the refractive index of the cladding material. Figure 4-2 illustrates total internal reflection inside an optical fiber. θ_c is the critical angle and is calculated by the following equation:

$$\sin(\theta_c) = n_2/n_1 \qquad \text{(Eq. 4-1)}$$

where n_1 is the index of refraction of the core and n_2 is the index of refraction of the cladding.

According to Snell's Law, the following equation applies for light entering the optical fiber from air with a refractive index of 1:

$$\sin(\theta_a) = n_1 \sin(\theta'_c) \qquad \text{(Eq. 4-2)}$$

The same equation applies for light exiting the optical fiber into air with a refractive index of 1. Therefore, an important feature of light transmission through an optical fiber is that light will enter and exit the fiber at the same angle. The numerical aperture (NA) of the optical fiber is defined as:

$$\text{NA} = \sqrt{{n_1}^2 - {n_2}^2} \qquad \text{(Eq. 4-3)}$$

The core diameter and numerical aperture are factors that affect the illumination. Specifically, the core diameter affects the packing fraction of the bundle and therefore the light-coupling efficiency. For example, a fiber with a large core diameter increases the packing fraction of the bundle of a fixed diameter compared to a smaller core diameter. This results in higher coupling efficiency when the fiber is coupled to the light source. Increasing the numerical aperture also increases the light collection efficiency, since the light collection is proportional to the numerical aperture squared [36].

One advantage of using fiber bundles for illumination is that the pattern of the bundles can be arranged at the distal end of the endoscope. Patterns such as a ring or a line can be used

for special imaging applications where specific illumination patterns are necessary. The ends of the fiber bundle can also be connected to optical splitters that branch the bundle into bifurcated to trifurcated bundles. The fibers in the fiber bundle are incoherent (not arranged in a particular order), which increases uniformity of the illumination. To obtain more uniform illumination, the fiber bundle can be split two or more groups and arranged symmetrically in a ring pattern. A wider field of illumination can be obtained by randomizing the direction of the fiber at the distal end by either bending or twisting the fiber bundle. Due to the length and spectral response of the fiber, a significant amount of light may be loss due to coupling and absorption. Increasing the power intensity of the light source can compensate for the loss of light.

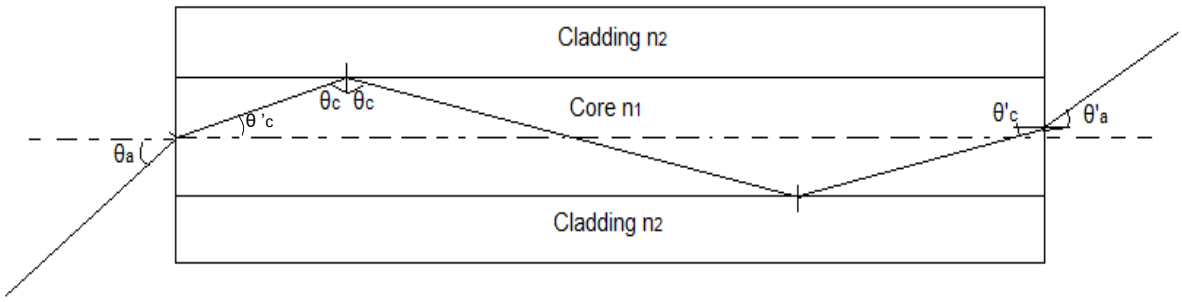

Figure 4-2. Total internal reflection inside an optical fiber.

4.2.2. Illumination Optics

The fiber bundle can be used in the illumination system without any additional optical components such as lenses. However, a set of lenses, such as aspheric lenses, can be used to achieve more uniform and a larger field of illumination. When imaging through fluid media such as blood, the illumination must be at a higher power than the normal emitted background in order

to produce enough reflected light for imaging. Any reflected light from the illuminated area enters the objective lens of the endoscope. The amount of light that reaches the observer depends on the following factors: intensity of the indecent light from the source, optical properties of the observed area, and the efficiency of the objective and image relay system.

The illumination of the imaging field affects the brightness of the observed image. Assuming that the field of view is circular, the amount of light that is captured by the endoscope can be calculated by the following equation [37]:

$$\Phi = LR(\pi y_o^2)(\pi \sin^2 \alpha), \quad \text{(Eq. 4-4)}$$

where L is the radiance from the fiber bundle, R is the reflection coefficient, y_0 is the height of the object, and α is the angle of the cone of incoming light that enters the objective lens. The πy_0^2 term represents the area of the observed object, while $\pi \sin^2 \alpha$ is the on-axis angle of the cone of incoming light rays. The angle of the cone, α, can be calculated by the following equation [36]:

$$\sin \alpha = \frac{p}{z}, \quad \text{(Eq. 4-5)}$$

where p is the radius of the entrance pupil of the objective lens and z is working distance. Equation 4-4 can be rewritten as by substituting in Equation 4-5 [36]:

$$\Phi = \pi^2 LR y_o^2 \left(\frac{p}{z}\right)^2. \quad \text{(Eq. 4-6)}$$

Therefore, the total amount of light that the endoscope receives from the imaging field is directly proportional to the radiance L and inversely proportional to the square of the working distance z. Equation 4-6 can also be rewritten in terms of the optical variant of the object space, H, and the refractive index n [36]:

$$\Phi = \frac{\pi^2 LR}{n^2} H^2 \quad , \qquad \text{(Eq. 4-7)}$$

where $H = n \sin(\alpha) y_0$. Therefore, the total amount of light that the endoscope receives from the imaging field is proportional to H^2. Figure 4-3 illustrates the operation of the distal end of an endoscope and the parameters in Equations 4-4, 4-5, 4-6, and 4-7.

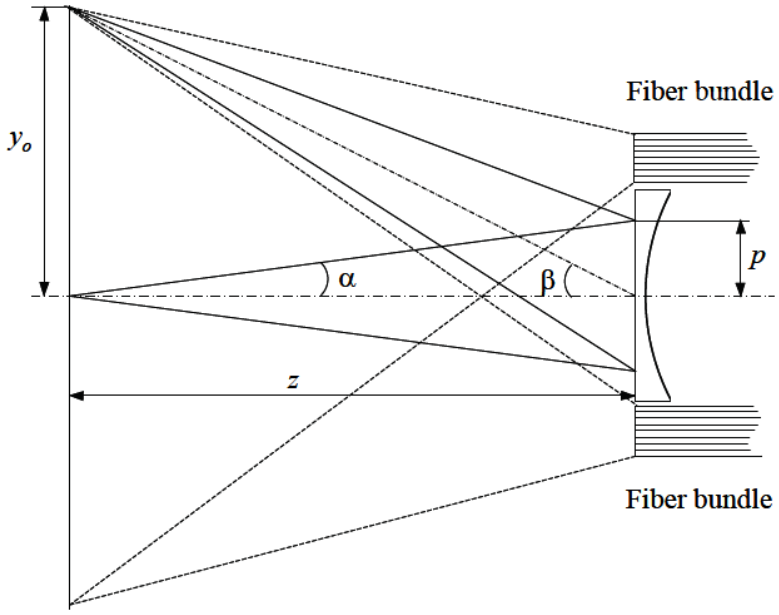

Figure 4-3. Imaging optics at the distal end of an endoscope. The light source is emitted from two fiber bundles. After light is reflected from the surface, it is captured by the objective lens [36].

4.3 Image Transmission System

4.3.1 Objective Lens

The purpose of the objective lens is to provide a high-quality image of the object to the relay system. The characteristics of an objective lens include a large field of view, large depth of field, and a high degree of telecentricity. The retrofocus lens is the most commonly used objective lens in rigid endoscopes and satisfies these criteria. It consists of two lenses (a front group and a rear group) and an aperture stop in between (Figure 4-4). The aperture stop is located at the front focal point, so that the chief rays are parallel to the optical axis. This is done in order to maximize the coupling efficiency of any off-axis rays into the relay system. To obtain the maximum field angle, the front lens group has a negative refractive power and consists of only one negative lens that determines the power of the objective lens. In contrast, the rear group has a positive refractive power and may be composed of multiple lenses.

The first element, which is the window of the objective lens, should be made from a very durable material. The window usually has a flat front surface in the direction of the tissue that is being imaged. This geometry is used in order to avoid changes in the optical power when the endoscope is immersed in blood. The optical invariant in the plane of the entrance pupil is calculated by the following equation [36]:

$$H = n \sin(\beta) p \,, \qquad \text{(Eq. 4-8)}$$

where β is the field angle and p is the radius of the entrance pupil. Therefore, given the H and the field of view, the β and the p can be obtained from Equation 4-8. Also, given the field of view, the focal length of the objective lens can be calculated by the following equation [36]:

$$f \tan(\beta) = r \quad , \qquad \text{(Eq. 4-9)}$$

where r is the radius of the aperture of the relay lens.

Another type of objective lens is the GRIN objective lens. GRIN lenses are an alternative to conventional lenses and utilize the continuous change in the refractive index of the lens material. In other words, the light rays are continuously bent within the lens until they are focused at a particular location. The advantage of a single element objective is that it decreases the tight tolerance requirement for the optical and mechanical components, significantly reducing the time and difficulty of assembling complex optical systems. Another advantage of a GRIN lens is that it only has two air-glass interfaces, which minimizes Fresnel reflection loss. However, a limitation of GRIN lenses is that the field of view is less compared to the objective lens in conventional endoscopes. Also, GRIN lenses suffer from significant dispersion, which makes it difficult to produce color corrected objective lens for visible imaging.

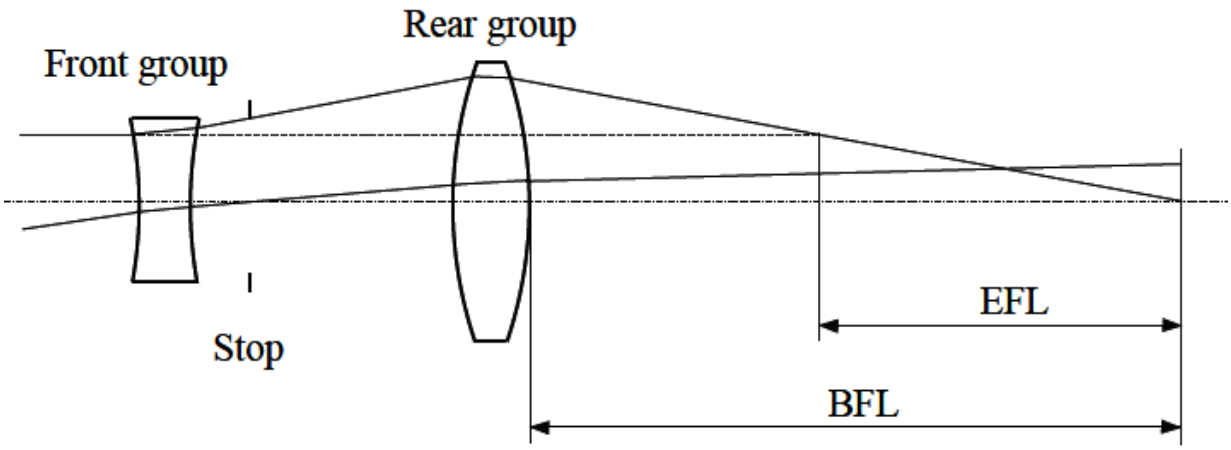

Figure 4-4. Diagram of a retrofocus objective lens system. The back focal length (BFL) is greater than he effective focal length (EFL) [36].

4.3.2 Conventional Relay

In a conventional relay image transmission system, several relay stages are used to transfer the image from the distal end of the endoscope to the proximal end. Each stage of the conventional relay system is telecentric in both the object and the image space. To satisfy this requirement, each half stage of the relay system consists of a relay objective lens and a field lens (Figure 4-5). These lenses are first mounted inside shorter thin tubes, and then slid inside of the rigid outer tube of the endoscope. The relay objective lens provides the magnification and numerical aperture, while the field lens provides the telecentric requirement.

The light intensity of the image in a rigid endoscope is determined by the optical invariant of the relay, H, which is related to the diameter of the relay lens and the numerical aperture. H is calculated by the following equation [36]:

$$H = n_o \sin(\alpha_o) y_o = n_i \sin(\alpha_i) y_i \,, \qquad \text{(Eq. 4-10)}$$

where n_0 and n_i are refractive indices of the objective lens and relay lens respectively, α_0 and α_i are the ray angles of the objective and image respectively, and y_0 and y_i are the height of the object and image respectively (Figure 4-6). The optical invariant of the relay system must be equal to that of the objective, so that the relay system can transmit the entire image created by the objective lens.

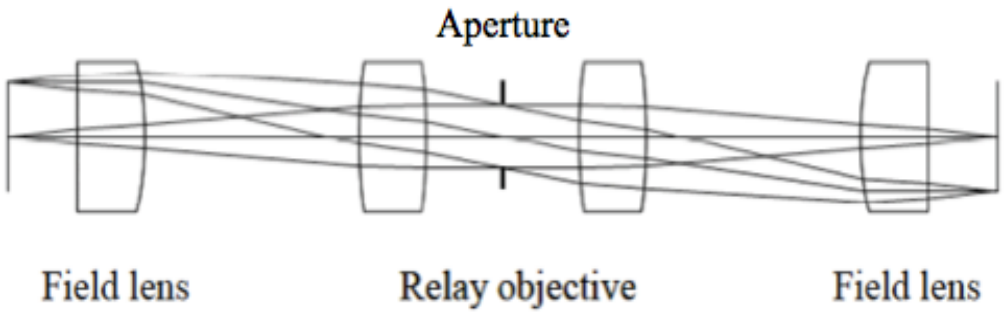

Figure 4-5. Diagram of an example conventional relay system [36].

Sin(α_i) and y_i from Equation 4-10 are at their maximum values at d/t and d respectively. Therefore, the maximum optical invariant, which represents the maximum light transmission, can be calculated by the following equation [36]:

$$H = n_i \sin(\alpha_i) y_i = n_i \left(\frac{d}{t}\right) d = n_i \frac{d^2}{t}, \quad \text{(Eq. 4-11)}$$

where t is the distance between the image and the entrance pupil of the relay lens and d is radius of the relay lens. Substituting Equation 4-11 into Equation 4-8, the maximum light that can be transmitted by the relay system is [36]:

$$\Phi = \left(\frac{\pi^2 LR}{n_o^2}\right) H^2 = \left(\frac{\pi^2 LR}{n_o^2}\right)\left(n_i \frac{d^2}{t}\right)^2 = \left(\frac{\pi^2 LR}{n_o^2 t^2}\right) n_i^2 d^4 \quad \text{(Eq. 4-12)}$$

.

According to Equation 4-12, the theoretical maximum light transmitted by the relay system is proportional to the square of the refractive index of the image and the forth power of radius of

the relay lens. However, due to effects of absorption and reflection, the actual maximum light transmitted is less than the theoretical value. Applying AF coatings to the surfaces and decreasing the number of interfaces are methods that can increase the light transmission.

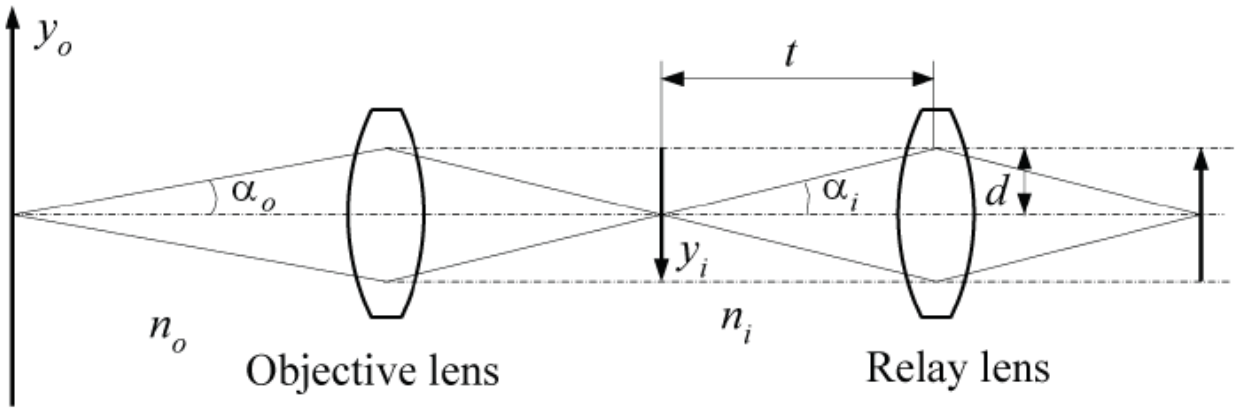

Figure 4-6. Diagram of objective and the first stage of an image relay system [36].

4.3.3 Gradient Index Lens Relay

A common relay system is the gradient index (GRIN) lens. GRIN lenses are an alternative to conventional relay lenses by utilizing the continuous change in the refractive index of the lens material. Thus, the light rays are bent in a sinusoidal path within the lens until they are focused at a particular location. The refractive index in the direction perpendicular to the optical axis can be expressed as:

$$n = n_0 \left(1 - \frac{k}{2}\right) r^2 \qquad \text{(Eq. 4-13)}$$

where n is the index of refraction, n_0 is the index of refraction at the center of the lens, k is the gradient constant, and r is the radius. The pitch, or length of one sinusoidal length, can be calculated by the following:

$$p = \frac{2\pi}{k} \qquad \text{(Eq. 4-14)}$$

where p is the pitch, and k is the is gradient constant.

The advantage of using GRIN relay lenses is that they can be manufactured to small thicknesses and diameters of approximately 0.2 mm and the outer surfaces of the lenses are finely ground to reduce stray reflection [36]. Compared to the numerical aperture of the conventional relay lens, the numerical aperture of the GRIN lens is larger. Also, the optical invariant of GRIN relay lenses is larger than that of conventional systems of equal diameter. Instead of complicated spherical or aspherical surfaces, which are typically found in conventional and Hopkins-rod lenses, GRIN lenses are plane surfaces. The advantage of plane optical surfaces allows for cost-effective production and a simplified assembly process. However, the disadvantage of a GRIN lens relay system in visible imaging is excessive dispersion, which makes it difficult to produce a color corrected relay system. The objective lens or focusing lens can correct the issue of overcorrected axial chromatic aberration.

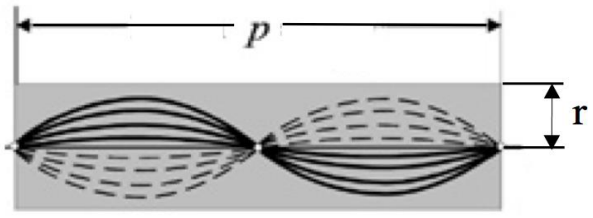

Figure 4-7. Example of GRIN rod lens. p is the pitch and r is the radius.

4.4. Summary and Conclusions

In this chapter, the basic principles of the illumination and imaging components in a conventional rigid endoscope were introduced. In fiber illumination systems, an incoherent fiber bundle transmits light from the light source to the region of interest at the distal end of the endoscope. The advantage of a fiber illumination system is that the fiber bundle can be used without any additional optical components such as lenses. For the imaging system, the GRIN lens system is much more cost effective and easier to assemble compared to other systems when the diameter of the optics is 2mm. Therefore, fiber illumination and a GRIN imaging system would be ideal for a rigid trans-blood imaging endoscope. In the next chapter, experiments and simulations demonstrating the feasibility of a rigid trans-blood imaging endoscope will be discussed.

CHAPTER 5:
SIMULATIONS AND EXPERIMENTS

5.1 Introduction

In this chapter, the results of optical sequential ray tracing simulations for the imaging system and non-sequential ray tracing for the illumination system will be discussed. The goal of the optical ray-tracing simulations and imaging experiments was to design and analyze a rigid catheter-based imaging and illumination system for intra-cardiac visualization in real-time through blood (Figure 5-1). Although the ability to image through blood has been previously investigated, the ability to image through blood using a rigid catheter has not been demonstrated in the literature. Compared to commercially available, fiber-optic systems, a rigid endoscopic system would be simpler in design, more durable, and lower in cost. Rigid endoscopes also offer higher resolution, wider viewing angles, and color reproduction compared to flexible endoscopes [38]. Another advantage of a rigid system is that smaller diameter lenses can be used, which decreases the diameter of the entire endoscope. This is especially important in pediatric patients, where the amount of space to work with is limited by the size of the patient's anatomy.

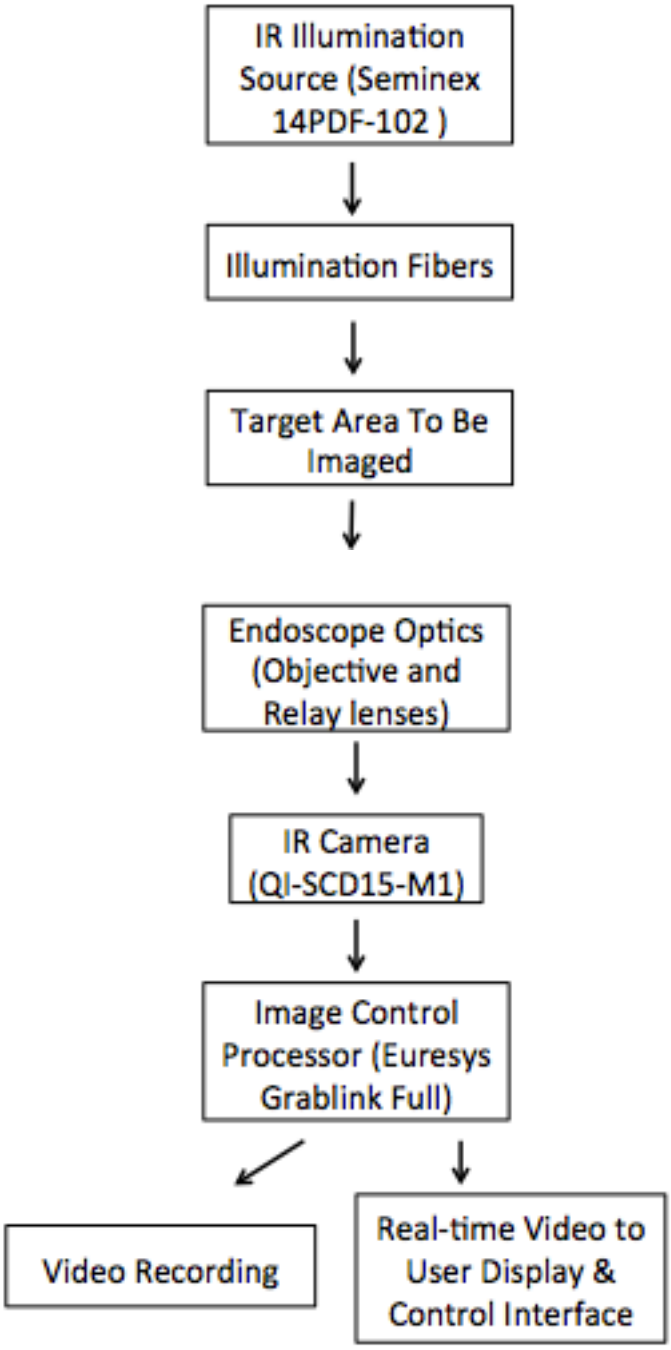

Figure 5-1. Block Diagram of Trans-Blood Imaging and Illumination System. The complete endoscopic system consists of the illumination system, relay optics, infrared camera, image control processor and video recording and display system.

5.2 Imaging System Design

5.2.1 Optical Lenses

Two different infrared endoscopic imaging systems were designed and evaluated for this thesis. The approach that was used to design the endoscopic imaging systems was to design the objective and relay systems together with the illumination system (Figure 5-1). System 1 is an infrared endoscope system designed entirely using GRIN lenses. The imaging system consists of a GRIN objective lens with a GRIN rod relay lens (Figure 5-2a). The GRIN lenses are manufactured using silver and lithium ion exchange on proprietary glass (GRINTECH, Jena, Germany) and are non-toxic and biocompatible (EN ISO 10993-1). The diameters of the GRIN objective lens and GRIN relay lens are 2 mm and the numerical aperture is 0.5 and 0.1 respectively. The GRIN objective lens has a design working distance of 20 mm and a length of approximately 5 mm. The length of the GRIN rod relay lens is approximately 178 mm. The objective and relay lenses are glued together with optical adhesive.

System 2 is an infrared endoscope system designed using a combination of GRIN and traditional lenses. The imaging system consists of a traditional objective lens system and GRIN rod relay lens (Figure 5-2b). The traditional endoscope objective in System 2 is a three-element telecentric objective lens system consisting of commercial plano-concave and plano-convex lenses. The diameters of the objective lenses range from 2 mm to 3 mm in diameter (Edmund Optics, Barrington, NJ). The GRIN rod relay lens is the same 2 mm diameter relay lens of that used in System 1. Both System 1 and System 2 have an eyepiece lens located at the proximal end of the endoscope that allows for the direct observation of the endoscope with an IR camera system.

A

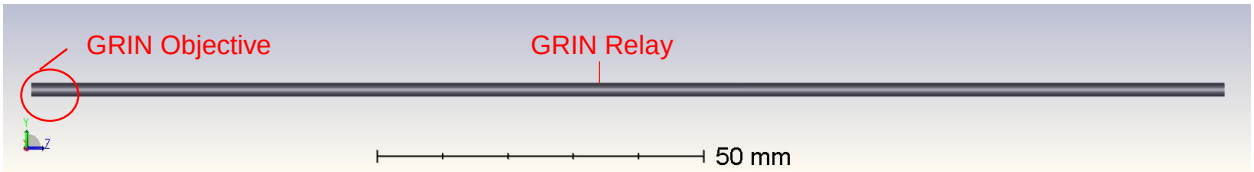

B

Figure 5-2. Shaded CAD models of two different imaging systems. A. GRIN Objective with GRIN Relay (System 1). B. Traditional Objective with GRIN relay (System 2).

5.2.2 Antireflective Coatings

An anti-reflective (AR) coating is a thin film layer of a quarter wavelength thickness that is applied to the surface of a lens to reduce Fresnel reflection. AR coatings decrease the amount of noise and ghost images on the imaging sensor caused by reflected and scattered light traveling backwards through the lens system. When light enters a lens with an anti-reflective coating, a ½ wave difference, or 180-degree phase shift, between the light reflected at the upper and lower boundary of the thin film occurs. The phase shift creates the conditions for destructive inference between the reflected beams, which leads to their cancellation before they exit the surface of the substrate. Transmission of light through the coating is dependent on several factors including: the wavelength of incident light, the index of refraction of the substrate, the index of refraction of the coating, the thickness of the coating, and angle of incidence of the light.

Since approximately 4% of the incident light passing through an uncoated glass will be reflected due to Fresnel losses [39], this loss becomes significant for System 2, where there are 5

lenses or 10 surfaces in the endoscope design. Therefore, approximately 0.96^{10}=0.664 or 66.4% of the light input for System #2 will reach the imaging sensor if absorption and scattering are neglected. To reduce the amount of reflection, the objective lens in System 1 is coated with a proprietary AR coating (GRINTECH, Germany) for 1550 nm and the objective lenses in System 2 are coated with either a Telecom-NIR AR coating or NIR II AR coating (Edmund Optics, Barrington, NJ). The wavelength range for the Telecom-NIR AR coating is 1200-1600nm, and 750-1550 nm for the NIR II AR coating. The average reflection of the Telecom-NIR AR coating is ≤ 0.25% while the average reflection of the NIR II AR coating is ≤ 0.7% (Figure 5-3). Table 5-1 lists the AR coatings applied to each lens in System 1 and System 2.

Table 5-1. AR Coating applied to each lens

System	**Lens**	**AR Coating**
1	GRINTECH Objective	1550 nm
1	GRINTECH Relay	Uncoated
1	Edmund Optics #33944	Uncoated
2	Edmund Optics #67979	NIR II
2	Edmund Optics #45971	Telecom-NIR
2	Edmund Optics #45974	Telecom-NIR
2	GRINTECH Relay	Uncoated
2	ThorLabs ASL10142-C	1050-1700 nm

A

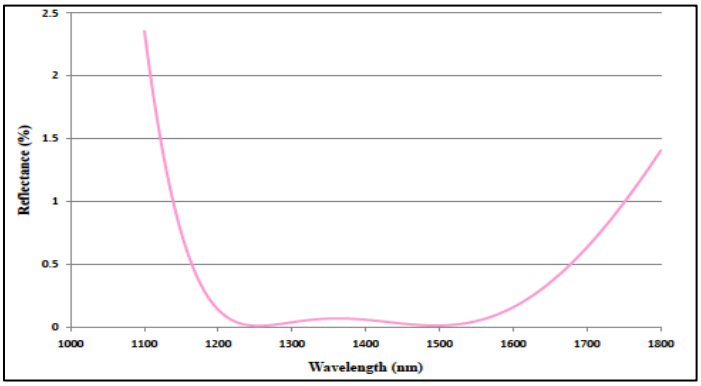

B

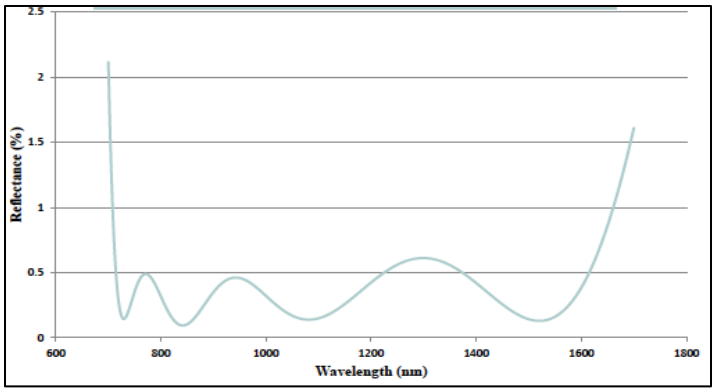

C

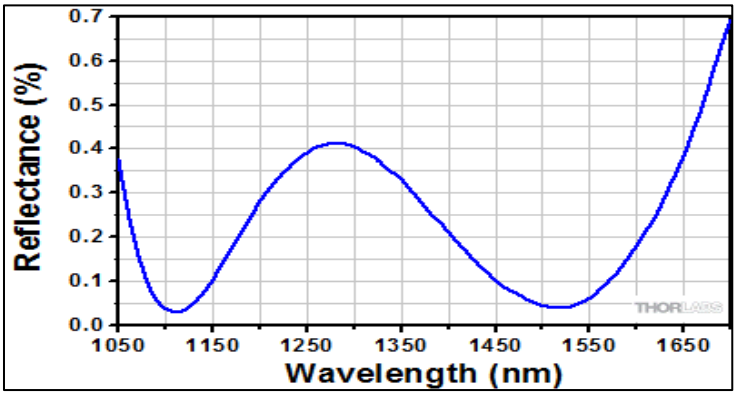

Figure 5-3. Reflectivity of AR Coatings as a function of wavelength. A. Edmund Optics Telecom-NIR AR Coating (1200- 1600nm) B. Edmund Optics NIR II AR Coating (750-1550nm) C. Thorlabs 1050-1700 nm Coating [39].

5.2.3 Infrared Camera

Besides lenses, the imaging sensor is another component of the imaging system. The imaging sensor of a compact c-mount infrared camera is located at the proximal end of the endoscope imaging system (Figure 5-4). The imaging sensor is an Indium-Gallium-Arsenide 640 x 512-pixel focal plane array with a pixel size of 15 um x 15 um (Model: QI-SCD15-M1, Quantum Imaging, Colorado Springs, CO). The specifications of the focal plane array include a dynamic range of 70dB, spectral response of 0.5um to 1.7um, and a frame rate of 30-60 frames per second (Figure 5-5). Imaging data from the camera was captured via a CameraLink cable using a Grablink Full frame grabber (Euresys, San Juan Capistrano, CA) installed on a PCI port of a computer. The infrared camera was evaluated and chosen based on the analysis of 2D Fast Fourier Transforms (FFT) using MATLAB (Mathworks, Natick, MA).

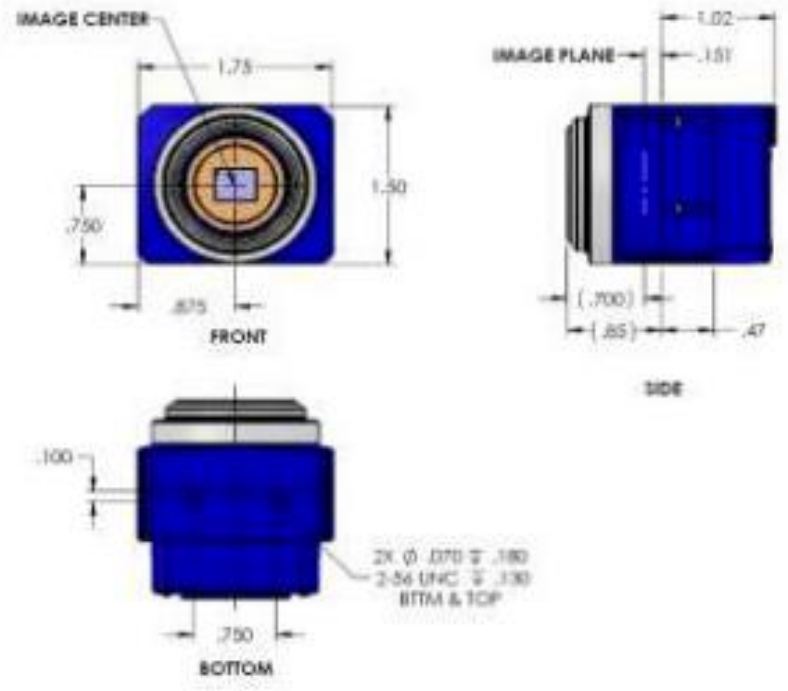

Figure 5-4. Mechanical Dimensions of the QI-SCD15-M1 SWIR Camera.

A

PARAMETER	VALUE	COMMENTS
Sensor Type	InGaAs	
Sensor Readout mode	Full Frame	snapshot
Image Format	640x512	640x480 in NTSC
Pixel Size	15um x 15um	
Active Area	100% fill factor	
Spectral Response	0.5um to 1.7um	See QE plot
Read Noise	<40 e rms	
Total Noise	<60 e rms	25°C sensor temp
Max Frame Rate	30 - 60 FPS	Consult QI for higher frame rates
Dynamic Range	70dB	typical
Power Dissipation	5 Watts	Typical at 30°C case

B

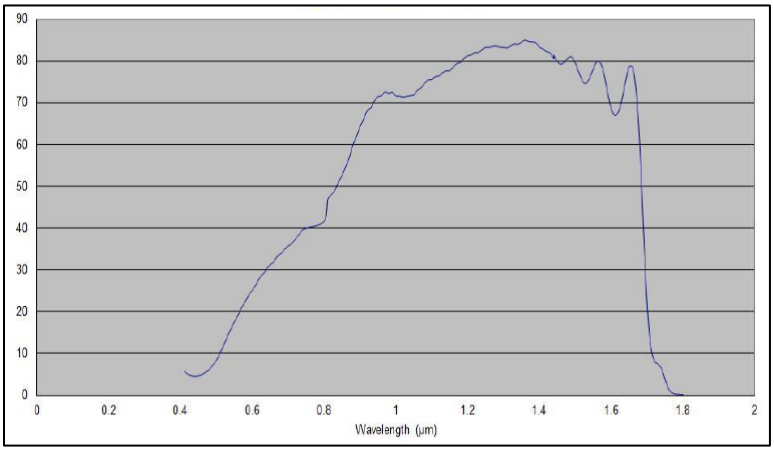

Figure 5-5. Specifications and spectral response for the QI-SCD15-M1 SWIR camera.

A. Camera and Sensor Specifications. B. Quantum Efficiency plot of the spectral response. The spectral response is greater than the IR region that the imaging system was designed for.

5.3 Camera Evaluation

The purpose of the camera evaluation was to determine the optimal infrared camera to use with the endoscopic imaging system. The criteria that were used to evaluate the cameras include high dynamic range and low readout and random noise images. Readout noise was evaluated because the noise is periodic and not randomly generated noise. Unlike random noise, periodic noise is more difficult to reduce with simple image processing techniques such as combing multiple images. When multiple images with periodic readout noise are combined, it reinforces the noise patterns. Other imaging processing techniques that remove non-random noise will do so at the cost of simultaneously eliminating some information from the original signal. Since readout noise cannot be removed, it decreases the signal to noise ratio of the imaging system and the dynamic range of the final image. Other limitations of readout noise include lower contrast images and undesirable visible patterns on the image.

Two different commercial infrared cameras were evaluated for the camera evaluation, the Quantum Imaging QI-SCD15-M1 and the Xenics Bobcat 640 CL (Xenics, Beverly, MA). To analyze the images, FFT plots were generated from random images taken with the infrared cameras. The following scripts were used to produce the FFT plots using MATLAB:

```
function w=window2(N,M,w_func)

wc=window(w_func,N);
wr=window(w_func,M);
[maskr,maskc]=meshgrid(wr,wc);
 w=maskr.*maskc;

end
```

This function is defined to remove edge effects when the FFT plot is produced in the following function.

```
function [ output_args ] = mywindow2( filename )

matrix = imread(filename);
matrix=im2double(matrix);
matrix_min= min(min(matrix));
matrix_max= max(max(matrix));
gray_image = mat2gray(matrix, [matrix_min matrix_max]);
imshow(gray_image);
[r,c]=size(gray_image);
w=window2(r,c,@hanning);
transform= fft2(gray_image.*w);
transform(1,1)= mean2(abs(transform));
invtransform = ifft2(transform);
figure;
imshow(invtransform);
IM = fft2(invtransform);
IM(1,1) = mean(mean(IM));
IM = fftshift(IM);
IM=abs(IM);
IM = IM/max(max(IM));
figure;imagesc(10*log10(IM));colormap jet(256);colorbar;caxis([-
50 0]);


end
```

As seen in Figure 5-5, the FFTs of the images taken using the QI infrared camera have smooth variation of pixels with one bright pixel at the center (Figure 5-6). The bright pixel at the center of the FFT plot is known as the “DC term” which represents the average intensity across the entire image. The lack of a visible horizontal or vertical pattern on the FFT is indicative of purely random Gaussian noise (Figure 5-6a). The Xenics Bobcat 640 CL infrared camera is a competing camera that was also compared by evaluating and analyzing the FFT. The lines in the FFT of the Bobcat 640 CL represent a pattern in the original image perpendicular to the line in the FFT. Although the structure of the noise was not seen in the original image, the structure of the noise can be easily seen in the frequency domain (Figure 5-6b). The vertical line in the FFT indicates horizontal noise of various frequencies in the original image and the horizontal line in the FFT indicates vertical noise of various frequencies in the original image. Also, compared to the FFT of the Quantum Imaging camera, the FFT of the Bobcat 640 CL Camera is less smooth. Therefore, the Quantum Imaging camera was selected for the imaging system because it introduced less measurable periodic read noise compared to the Bobcat 640 CL.

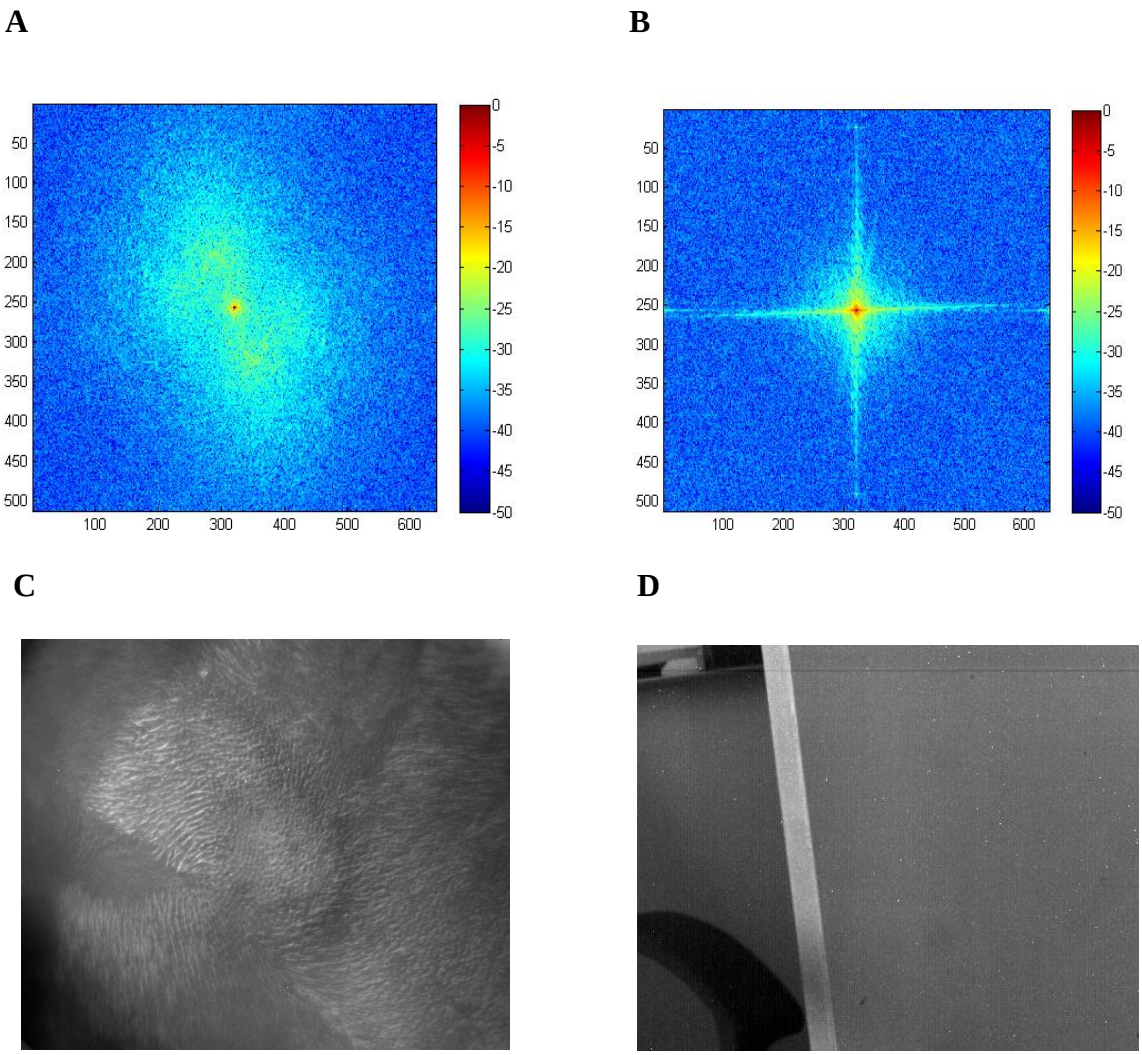

Figure 5-6. Fast Fourier Transform of Infrared Images. A. FFT of image captured using the Quantum Imaging QI-SCD15-M1 camera. B. FFT of infrared image captured using the Xenics Bobcat 640 CL camera. C. Original image used to compute the FFT for Fig. 5-4a. D. Original image used to compute the FFT for Fig. 5-4b.

5.4 Sequential Ray-Tracing Simulations

5.4.1 System Setup

Optical ray-tracing simulations for two different systems, System 1 and System 2, were performed in OpticStudio 15.5 in sequential ray-tracing mode. The wavelengths for both systems were set to 1450-1650 nm (the primary wavelength was set to 1550 nm) and the field positions were set to 0-30 degrees. Lens prescriptions for System 1 and System 2 were entered into the lens data editor to specify the radius of curvatures, thickness, lens material, and coatings for each optical surface (Figure 5-7).

Each imaging system was optimized using the optimization feature. The variables that were optimized included the radii of curvature, lens thicknesses, and air thicknesses. The default merit function editor for optimization was set to "root-mean-square" of the "spot radius" relative to the "centroid." The pupil integration of the default merit function editor was set to Gaussian Quadrature with "6 rings," and "3 arms."

5.4.2 Lens Stock Matching Tool

The Lens Stock Matching tool converted the fictitious glasses into real glasses in the Edmund Optics lens catalog to minimize material costs by eliminating the need for manufacturing custom made lenses. The Lens Stock Matching tool works by matching lenses to the nearest equivalents in the catalog of pre-selected vendors. The effective focal length tolerance and entrance pupil diameter tolerance were both set to 25% in the settings of the Lens Stock Matching tool. The lenses that were selected included plano-curved and equi-curved with anti-reflective coatings. The catalog number of each matched lens is listed in the "Comments" column of the Lens Data Editor (Figure 5-7).

A

	Surf:Type		Comment	Radius	Thickness	Material	Co	Clear Semi-Dia	Chip Zone	Mech Semi-Dia	Conic	TCE x 1E-6	Par 1(unused)	Par 2(unus	Par 3(unused)	Par 4(unused)
0	OBJECT	Standard		Infini...	20.000			9.326	0.000	9.326	0.000	0.000				
1	STOP (aper)	Gradient 5	IFRL-200-020-50	Infini...	5.056	GTAGNEU		1.000 U	-	-	0.000	0.000	0.050	1.629	-0.085	3.154E-03
2	(aper)	Standard		Infini...	0.000			1.000 U	0.000	1.000	0.000	0.000				
3	(aper)	Gradient 5	IFRL-200-125-10	Infini...	177.771	GTRY		1.000 U	-	-	0.000	0.000	0.300	1.605	-3.067E-03	4.763E-06
4	(aper)	Standard		Infini...	1.000			1.000 U	0.000	1.000	0.000	0.000				
5	(aper)	Even Asphere	33944	29.457	5.500	L-BAL35		11.250 U	1.250	12.500	-0.710	-	0.000	5.840E-...	0.000	0.000
6	(aper)	Standard		Infini...	60.970 M			12.000 U	0.500	12.500	0.000	0.000				
7		Standard		Infini...	-2.634 V			5.362	0.000	5.362	0.000	0.000				
8	IMAGE	Standard		Infini...	-			5.090	0.000	5.090	0.000	0.000				

B

	Surf:Type		Comment	Radius	Thickness	Material	Coating	Clear Semi-Dia	Chip Zone	Mech Semi-Dia	Conic	TCE x 1E-6	2nd Order Ter	4th Order Ter	6th Order Ter	8th Order Ter
0	OBJECT	Standard		Infinity	20.000			9.704	0.000	9.704	0.000	0.000				
1	(aper)	Standard		Infinity	1.000	N-SF11		1.500 U	0.000	1.500	0.000	-				
2	(aper)	Standard	67979	4.710	0.245		NIRII	1.500 U	0.000	1.500	0.000	0.000				
3	STOP	Standard		Infinity	0.529			0.335	0.000	0.335	0.000	0.000				
4	(aper)	Standard		Infinity	0.800	LASFN9	ZEC_TELECOMNIR5...	1.000 U	0.000	1.000	0.000	-				
5	(aper)	Standard	45971	-1.700	0.725		ZEC_TELECOMNIR5...	1.000 U	0.000	1.000	0.000	0.000				
6	(aper)	Standard	45974	2.255	0.800	LASFN9	ZEC_TELECOMNIR5...	1.000 U	0.250	1.250	0.000	-				
7	(aper)	Standard		Infinity	0.939		ZEC_TELECOMNIR5...	1.000 U	0.250	1.250 U	0.000	0.000				
8	(aper)	Gradient 5	IFRL-200-125-10	Infinity	177.771	GTRY		1.000 U	-	-	0.000	0.000	0.300	1.605	-3.067E-03	4.763E-06
9	(aper)	Standard		Infinity	1.000			1.000 U	0.000	1.000	0.000	0.000				
10	(aper)	Even Asphere	ASL10142-C	35.826	6.000	C79-80	THORC	12.700 U	0.000	12.700	-0.629	-	0.000	1.440E-07	0.000	0.000
11	(aper)	Standard		Infinity	92.772 M			12.700 U	0.000	12.700	0.000	0.000				
12		Standard		Infinity	-5.818 V			5.475	0.000	5.475	0.000	0.000				
13	IMAGE	Standard		Infinity	-			5.071	0.000	5.071	0.000	0.000				

Figure 5-7. Lens prescription data for System 1 and System 2. A. GRIN Objective & GRIN Relay (System 1) B. Traditional Objective & GRIN Relay (System 2).

A

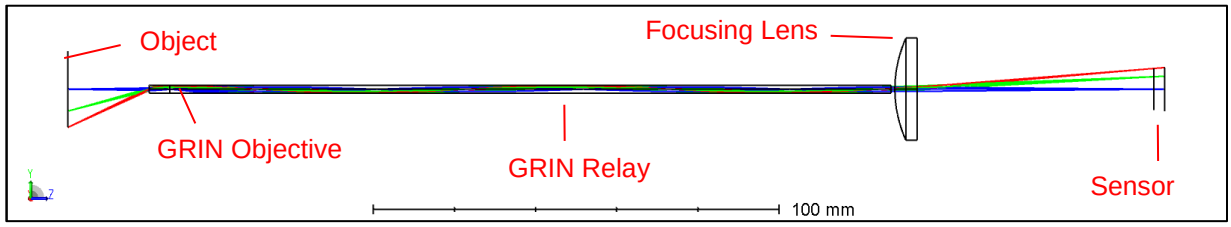

B

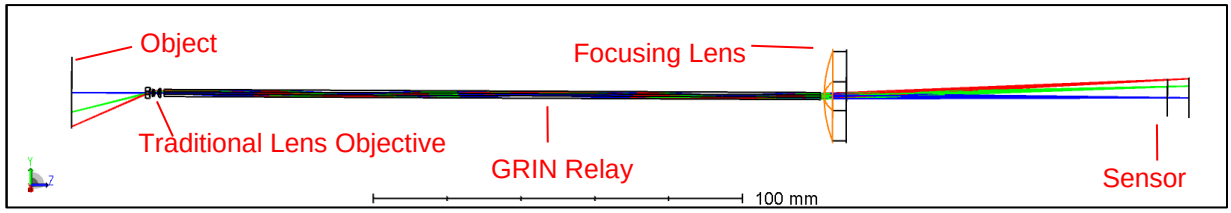

Figure 5-8. Cross-sectional layout of System 1 and System 2. A. GRIN Objective & GRIN Relay (System 1) B. Traditional Objective & GRIN Relay (System 2).

5.4.3 Cross-sectional Layout

The cross-sectional layout in Figure 5-8 shows that each imaging system consists of three components: the objective, relay, and the focusing lens. The image plane on the lens layout represents the location of the focal plane array of the IR camera. The image size is approximately the same size as the active area of focal plane array. Both System 1 and System 2 have a viewing distance of 20-30 mm, which is sufficient for intra-operative cardiac applications such as the placement of electrophysiological pacemakers, artificial valves, or RF ablation catheters [21]. The cross-sectional layout also shows that the objective lens of the imaging system fulfilled the image-space telecentric requirement, so that the chief ray of each imaging point is parallel to the optical axis. This is necessary to avoid vignetting when light is being transmitted through the relay lens from the distal end to the imaging sensor located at the proximal end. However, the disappearance of some rays indicate that some light was lost due vignetting because of the low NA of the relay lens. The lost light rays may get absorbed by the lens housing or become stray light that are reflected into the lens system, forming ghost images and reducing image contrast.

5.4.4 1st Order Optical Properties

The 1st order optical properties for each design are listed in Table 5-2. Both System 1 and System 2 have similar entrance pupil diameters. The entrance pupil diameters of System 1 and System 2 are 0.6 mm and 0.62 mm respectively. The effective focal length are 11 mm and 12 mm respectively, corresponding to an image space f/# of 17.7 and 19.9 respectively, and the image space NA for System 1 and System 2 are 0.025 and 0.024 respectively. The overall track length of System 2 is greater than System 1. For System 1, the overall track length is 250 mm and for System 2, the overall track length is 282 mm.

Table 5-2. 1st order optical properties for System 1 and System 2

Specification	**System 1**	**System 2**
Effective Focal Length (mm)	11	12
Back Focal Length (mm)	54	85
Total Track (mm)	250	282
Image Space F/#	17.74	19.9
Paraxial Working F/#	19.71	21.61
Working F/#	19.65	20.01
Image Space NA	0.025	0.023
Object Space NA	0.015	0.014
Paraxial Image Height (mm)	5.70	6.05
Paraxial Magnification	-0.611	-0.623
Entrance Pupil Diameter (mm)	0.62	0.6
Exit Pupil Diameter (mm)	3.42	4.36

A

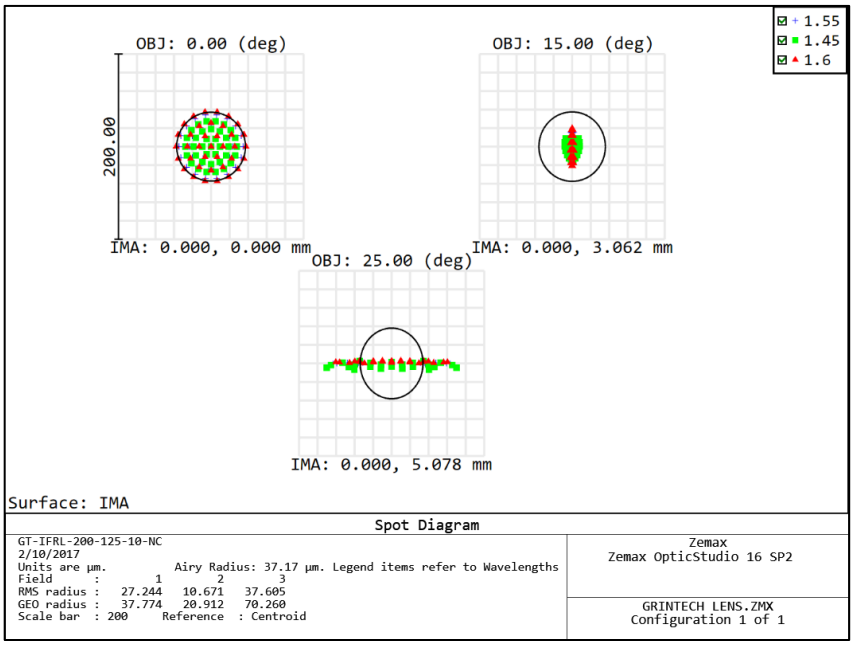

B

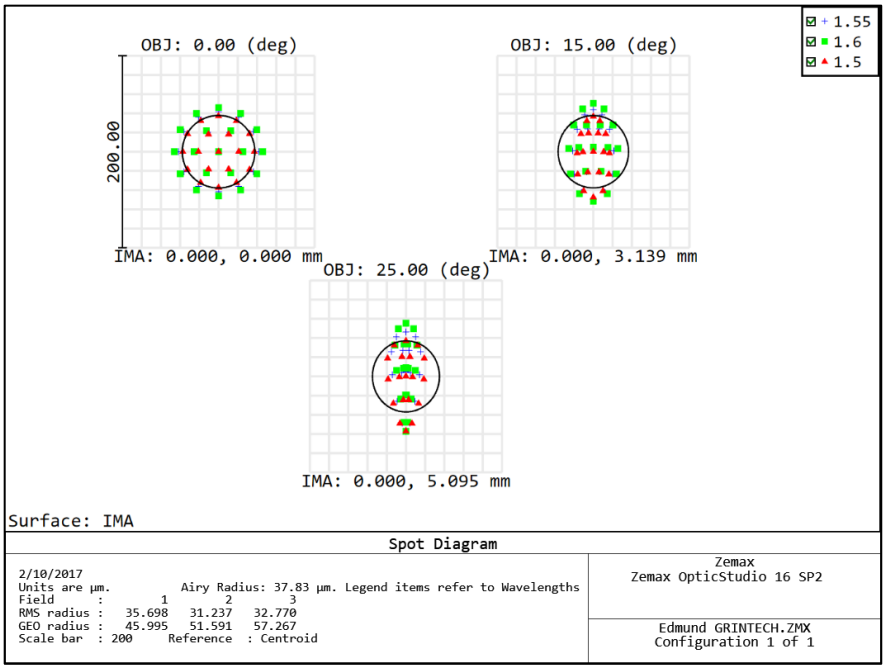

Figure 5-9. Standard spot-diagrams for three field positions. A. GRIN objective with GRIN Relay (System 1). B. Traditional Objective with GRIN Relay (System 2).

5.4.5 Standard Spot Diagram

The standard spot diagram presented in Figure 5-9 shows that the RMS spot size is either less than or approximately equal to the Airy disk radius over the entire field of view for both systems (Figure 5-9). An Airy disk is a circular light pattern formed from the image of a point object as a result of diffraction. The Airy disk radius limits the resolution of the imaging system and is calculated by the following equation:

$$r = \frac{1.22\lambda d}{D} \qquad \text{(Eq. 5-1)}$$

where D is the entrance pupil diameter, λ is the wavelength of light and d is the working distance.

Equation 5-1 shows that the Airy disk radius is inversely proportional to the entrance pupil diameter and directly proportional to the working distance and wavelength of light. Since, the Airy disk radius is limited by the entrance pupil diameter, it is also limited by the outer diameter of the endoscope lens. Additionally, since the Airy disk radius is proportional to the wavelength of light, the Airy disk radius of an infrared endoscope may be 2-3 times than that of a visible light endoscope. The Airy radius calculated for both System 1 and System 2 at 1550 nm is approximately 37 μm. Because the RMS spot sizes are similar to their respective Airy disk radius, the performances of both optical systems are limited by diffraction (Figure 5-9). Additionally, the RMS spot sizes and Airy disk radii are greater than the pixel pitch the focal plane array, which means that the high resolution-imaging sensor exceeds the imaging ability of the optical imaging system. Therefore, overall performance of the imaging system is limited by diffraction instead of the imaging sensor.

A

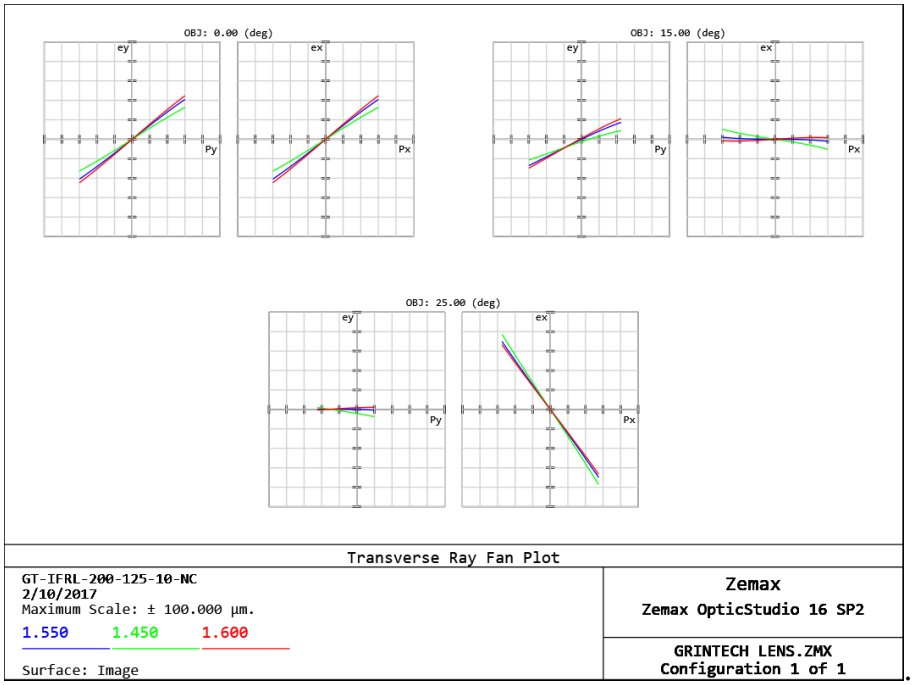

B

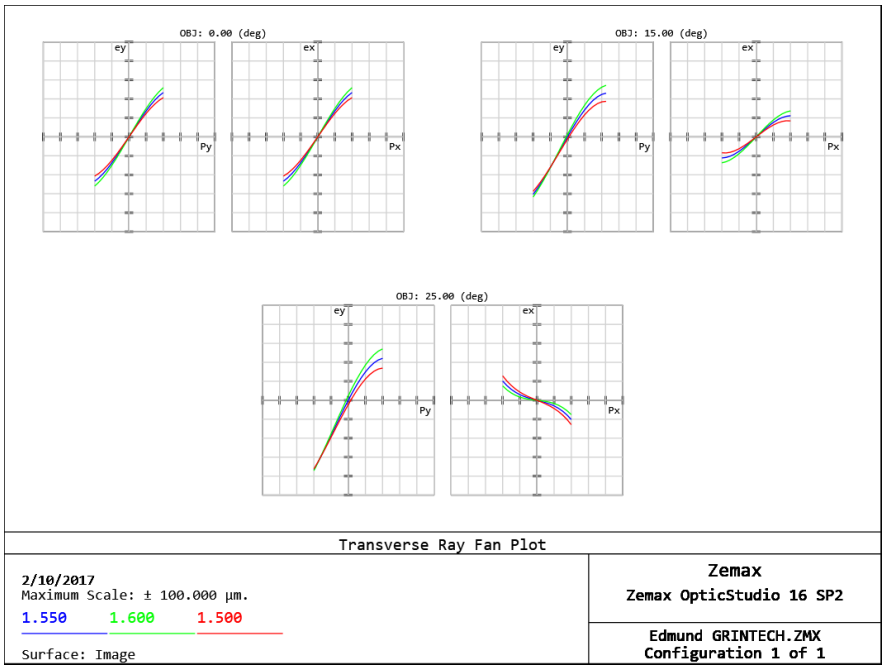

Figure 5-10. Transverse Ray Fan Plot for two different imaging systems. A. GRIN objective with GRIN Relay (System 1). B. Traditional Objective with GRIN Relay (System 2).

A

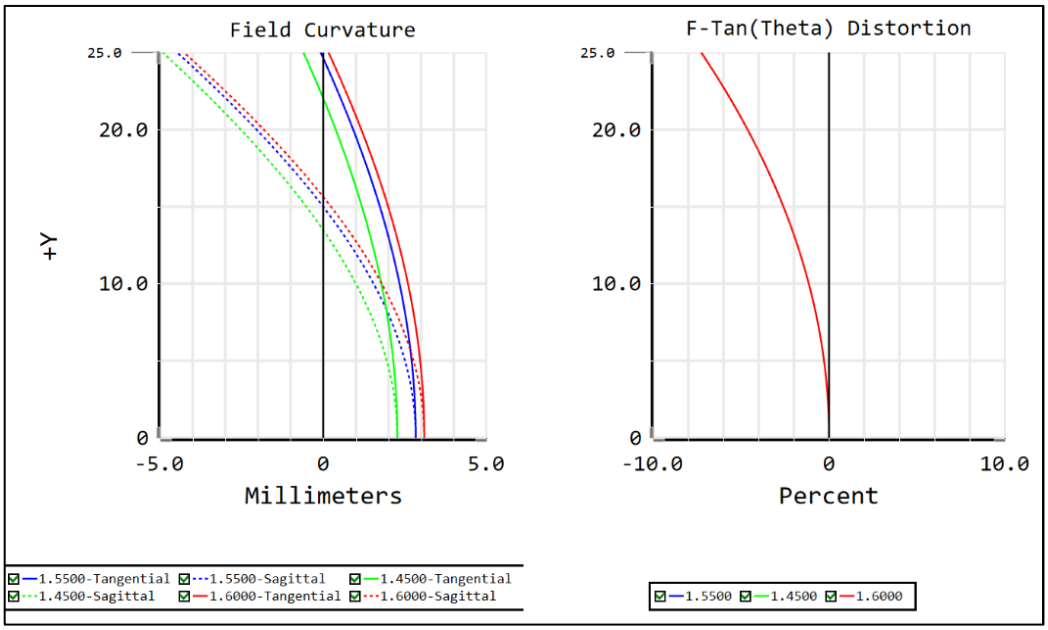

B

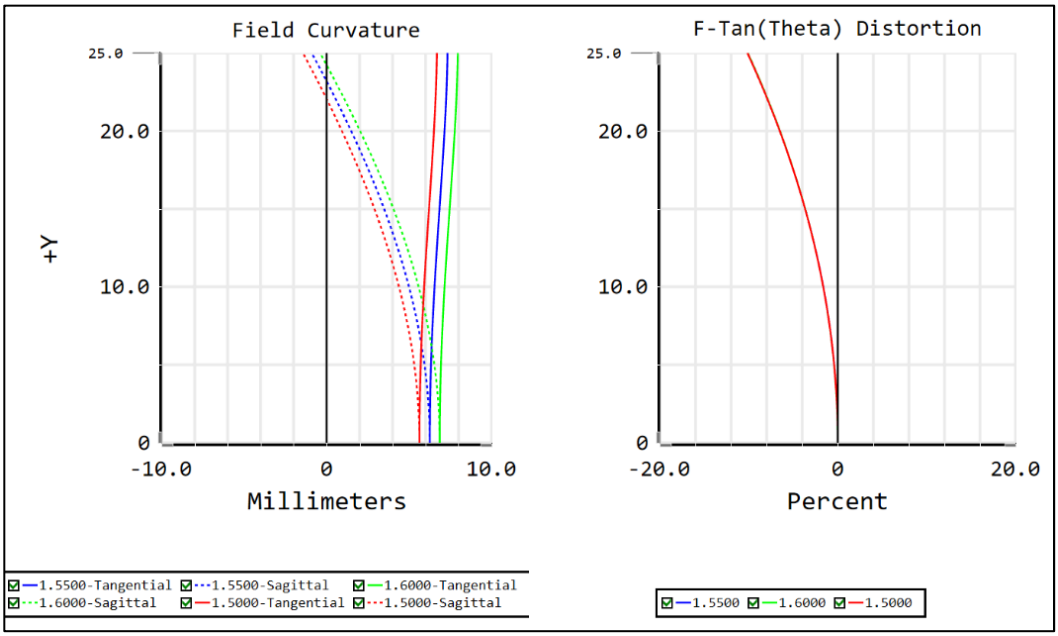

Figure 5-11. Field curvature and distortion plot for two different imaging systems. A. GRIN objective with GRIN Relay (System 1). B. Traditional Objective with GRIN Relay (System 2).

5.4.6 Transverse Ray Fan Plots

The transverse ray fan plots in Figure 5-10 show the aberrations of the two imaging systems as a function of wavelength and pupil coordinate. In System 1 and System 2, there is a large amount of defocus clearly indicated in both plots, depicted by the steep slope though the origin. While axial color and lateral color are minimal for both systems, System 1 has slightly more axial color than System 2, indicated by the differences in slope for the 1450 nm plot compared to that of other wavelengths. Spherical aberration is more prevalent in System 2 than in System 1, as indicated by the non-linear function. Astigmatism and coma is present in both System 1 and System 2 in the outer field. Astigmatism is indicated by the difference in slopes in the tangential and sagittal ray fans, while coma is indicated by asymmetry in the tangential plots.

5.4.7 Field Curvature and Distortion

The field curvature and distortion for both System 1 and System 2 are computed at several wavelengths ranging from 1450 to 1600 nm as a function of field angle (Figure 5-11). If the field curvature is large, only the area in the center of the image will be in focus while the peripheral areas of the image will be blurry. This would result in a smaller field of view and may cause eye fatigue for the physician who is using the endoscope. An optimal imaging system has a flat field with no field curvature. The field curvature plot in Figure 5-11 indicates that the amount of field curvature is similar for different field angles for both Systems 1 and System 2. However, the field curvature in the sagittal direction is greater than the field curvature in the tangential direction in both systems. Additionally, the field distortion plots in Figure 5-11 show that distortion is proportional to the field angle but is larger for System 2 compared to System 1. However, the distortion for both optical systems at the 30-degree field is less than -10%.

5.4.8 Wavefront Aberration Coefficients

The wavefront aberration, W, is another method used to consider the aberrations in real lens systems. Wavefront aberration is defined as the optical path length difference between the actual wavefront and the reference wavefront that is centered on a reference image point. For a rotationally symmetric optical imaging system, the wavefront aberration is defined by the following equation:

$$W = W_{020}\rho^2 + W_{111}H\rho\cos\theta + W_{040}\rho^4 + W_{131}H\rho^3\cos\theta + W_{222}H^2cos^2\theta + W_{220}H^2\rho^2 + W_{311}H^3\rho\cos\theta + \cdots \quad \text{(Eq. 5-2)}$$

where H is the normalized image height, θ is the azimuth angle, and ρ is the normalized pupil height.

Table 5-3. Wavefront aberration coefficients for System 1 and System 2

	W040	**W131**	**W222**	**W220**	**W311**	**W020**	**W111**
System 1	-0.235	0.066	0.539	0.041	12.58	-0.09	0.07
System 2	-0.236	0.197	-0.973	1.2	10.92	-0.14	-0.17

The wavefront aberration coefficients for System 1 and System 2 are listed in Table 5-3. W_{040} is the wavefront aberration coefficient for spherical aberration and is similar for both systems. The wavefront aberration coefficients for spherical aberration, astigmatism, field curvature, defocus and tilt, W_{131}, W_{222}, W_{220}, W_{020}, and W_{111} respectively, are greater for System 2 than those of System 1. However, W_{311}, the wavefront aberration coefficient for distortion, is greater for System 1 than that of System 1.

A

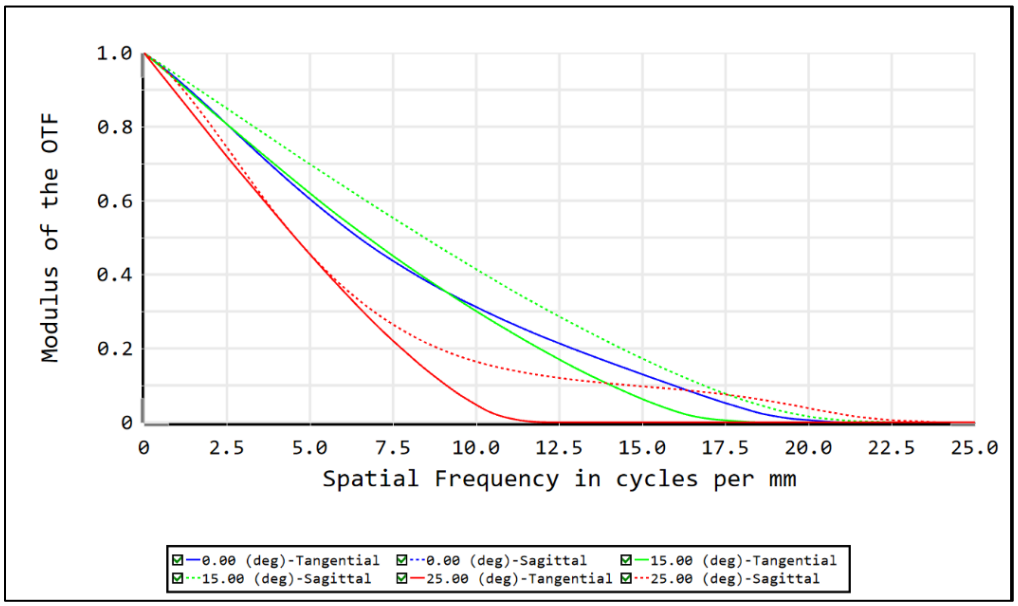

B

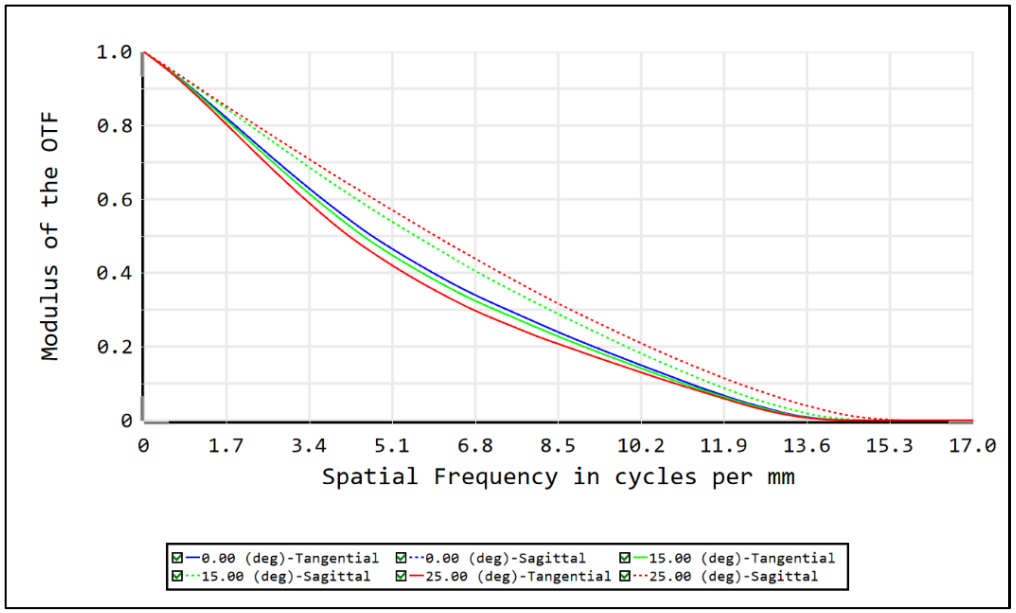

Figure 5-12. Polychromatic modulation transfer function curves for two imaging systems. A. GRIN objective with GRIN Relay (System 1). B. Traditional Objective with GRIN Relay (System 2).

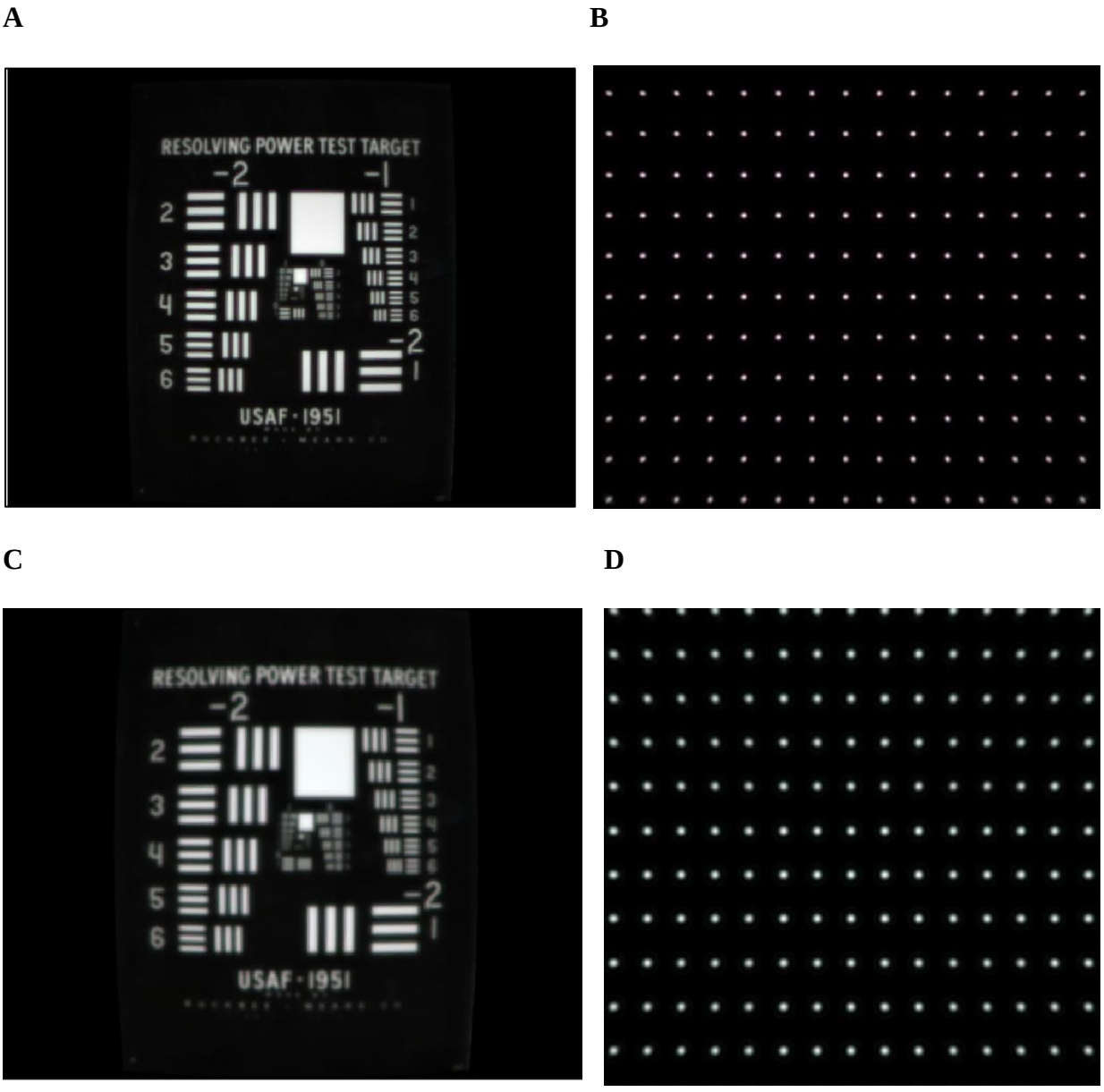

Figure 5-13. Image simulation of a negative USAF 1951 resolution test target for two different imaging systems. A. Simulated image of GRIN objective with GRIN Relay (System 1). B. Point Spread Function Plot of System 1. C. Simulated image of Traditional Objective with GRIN Relay (System 2). D. Point Spread Function Plot of System 2.

5.4.9 Modulation Transfer Function

The modulation transfer function (MTF) plots in Figure 5-12 describe the performance of the two imaging systems as a function of spatial frequency. The MTF is a measurement of the ability of an optical system to transfer the contrast of on object of a particular resolution to the image. It is defined as the ratio of the image contrast to the object contrast. For an aberration-free system, the cutoff frequency, which is the frequency where the MTF is zero, is calculated using the following equation:

$$f_{cutoff} = \frac{1}{\lambda(f/\#)} \qquad \text{(Eq. 5-3)}$$

where λ is the wavelength and f/# is the f-number. The aberration-free cutoff frequency for System 1 and System 2 calculated from Equation 5-3 is 32 cycles/mm. However, the cutoff frequency from the MTF plots is approximately 14 cycles/mm (Figure 5-12), which is significantly less than the aberration-free image cutoff frequency. Therefore, the difference between the two values is a result of aberrations present in both optical systems.

5.4.10 Image Simulation

The image simulation of a USAF 1951 resolution test chart is shown in Figure 5-13. The pixel size for the image simulations was 15 um with 640 x 512 pixels, which is the same size as the focal plane array. The resolution of the simulated images for both System 1 and System 2 is feasible for infrared imaging. The results of the image simulations show that the field of view for System 2 was greater than System 1. The half field of view for System 1 and System 2 was 35 and 37 degrees respectively. This difference in the field of view was expected, since GRIN objective lenses have a smaller field of view compared to traditional objective lens systems.

A

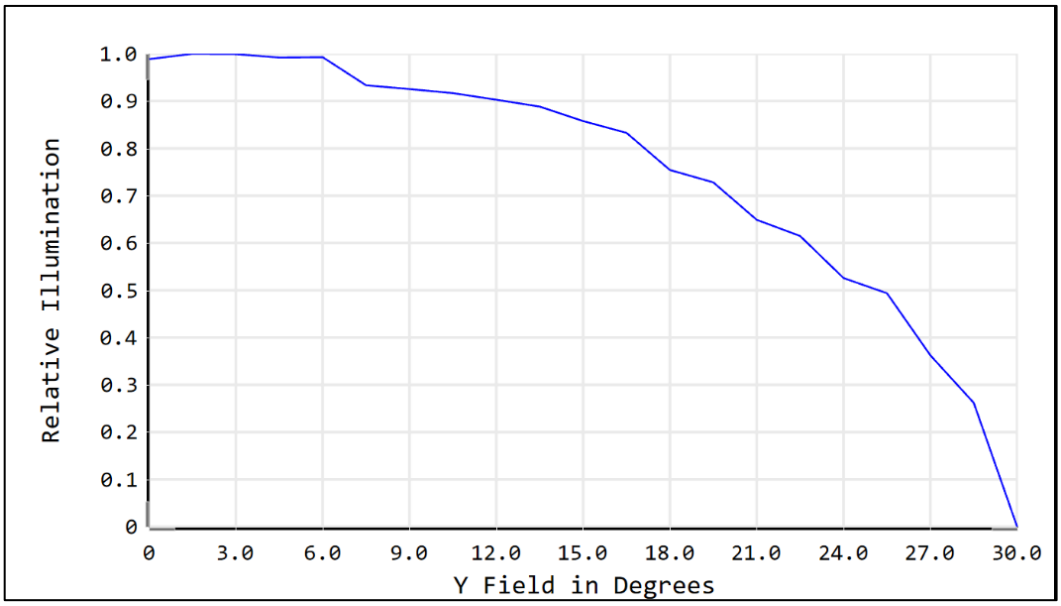

B

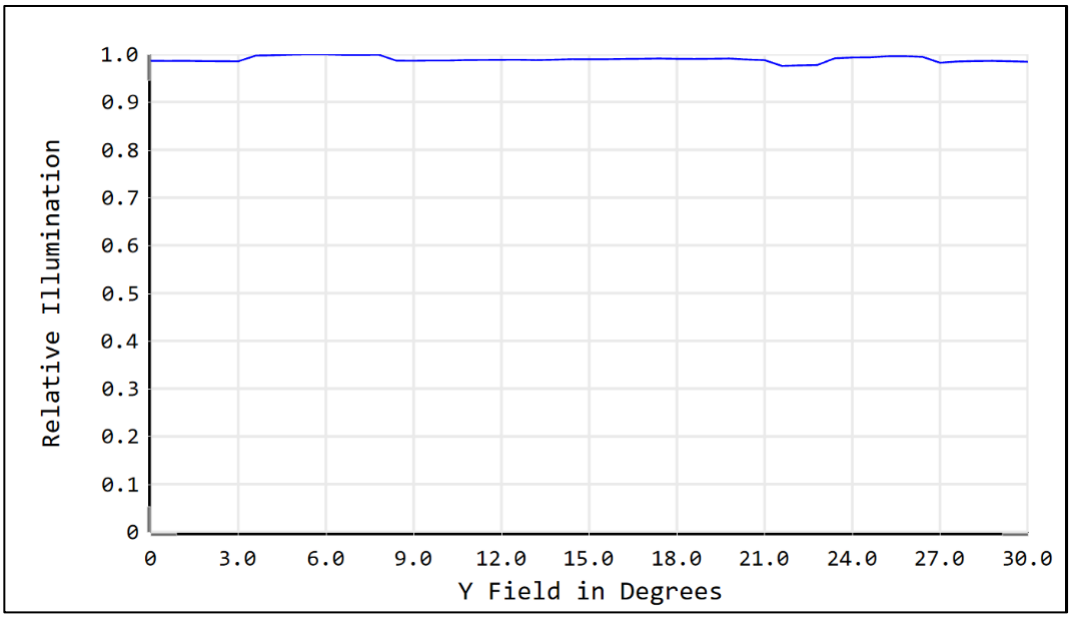

Figure 5-14. Relative illumination curve for two different imaging systems. A. GRIN objective with GRIN Relay (System 1). B. Traditional Objective with GRIN Relay (System 2).

5.4.11 Relative Illumination

The relative illumination curve shown in Figure 5-14 computes the relative illumination as a function of y field coordinate. Relative illumination is defined as the ratio of intensity of illumination per unit area of an image surface to the maximum illumination at any point in the field. It is computed by integrating the effective area of the exit pupil as seen from the image points. For System 1, the image center is the brightest portion of the image. The relative illumination decreases to zero as the field angle increases from the center to the edge of the field (Figure 5-14a). For System 2, the relative illumination is uniform; the relative illumination does not change significantly across the field of view (Figure 5-14b). The relative illumination is uniform because the objective lens design in System 2 has a larger field of view than that of System 1. However, due to the size of the focal plane array, the field of view for the entire endoscope system for System 2 is limited to 30 degrees.

5.4.12 Tolerance Analysis

Tolerance analysis was used to analyze the effects of manufacturing and alignment errors on the optical and mechanical components of the two imaging systems. Two different types of tolerance analyses were performed on each imaging system using the Tolerancing feature in OpticStudio: sensitivity analysis and Monte Carlo analysis. In sensitivity analysis, the change in the tolerancing criterion is computed separately for each extreme value of the optical parameter (radius of curvature, center thickness, index of refraction, etc.). RMS spot size was the tolerancing criterion that was considered for sensitivity and Monte Carlo analysis. In Monte Carlo analysis, the effects of all perturbations are analyzed simultaneously and repeated over numerous cycles. Every parameter with a specified tolerance is chosen randomly according to a statistical distribution for each Monte Carlo cycle. Each cycle represents one endoscope unit

produced in a manufacturing setting. By default, each of the parameters considered for tolerancing is assumed to follow a Gaussian distribution with a total width of four standard deviations from the minimum and maximum values. The sensitivity analysis and Monte Carlo simulation was performed on both System 1 and System 2 with the standard commercial and high-precision tolerances requirements listed in Table 5-4.

Table 5-4. Parameters used for Zemax tolerance analysis

Parameter	**Tolerance**
Radius	±0.01 mm
Thickness	±0.01 mm
Tilt	±0.5 arcmin
Decenter	±0.01 mm
Index	±0.0005
Abbe Number	±0.5%

The sensitivity and Monte Carlo tolerance analysis reports for System 1 and System 2 can be found in Appendix A. The results of the Monte Carlo simulations show that there is an 80% probability of obtaining an RMS spot size equal to 49 µm for System 1 and 64 µm for System 2 (Appendix A). Since System 2 has more optical lens components in the objective compared to System 1, System 2 would require much higher precision tolerances to obtain comparable performance to System 1. However, requiring higher precision tolerances for the lenses would significantly increase the manufacturing costs of the entire system, making System 2 less cost-effective compared to System 1.

5.5 Large Scale Objective Prototype

To demonstrate proof-of-concept, a large-scale traditional objective lens system was designed on OpticStudio 15.5 and assembled using commercial lenses and lens tubes (Edmund Optics, Barrington, NJ & Thorlabs, Newton, NJ). Table 5-5 lists the lenses and materials used to assemble the prototype (Table 5-5). The large-scale system is an 8:1 scale model of the traditional objective lens system found in System 2 (Figure 5-15a). To test the resolution of the system, a USAF 1951 test target was placed at its designed working distance of 80 mm (Figure 5-15b). The USAF 1951 test target is the industry standard to determine the optical resolution of endoscopes (ISO 8600-5) and was also simulated for comparison (Figure 5-15c). Images were displayed in real-time using the Multicam 6.11 frame grabber software and camera file provided by the manufacturer. The image of the test target was in focus and similar in resolution to the simulated image. Ghosting or other reflection artifacts were not observed (Figure 5-15d).

Table 5-5. Bill of Materials for Large-Scale Objective Prototype

Material	**Item #**	**Vendor**	**Price**
20 mm Dia. x -50 FL, Uncoated, Plano-Concave Lens	45024	Edmund Optics	$25
18 mm Dia. x 18 FL, Uncoated, Plano-Convex Lens	48423	Edmund Optics	$25.50
20 mm Dia. x 30 FL, Uncoated, Plano-Convex Lens	45239	Edmund Optics	$25.50
SM1 Lens Tube, 1.5" Thread Depth	SM1L15	Thorlabs	$15.70
Adapter with External M42 x 1 Threads and Internal	SM1A49	Thorlabs	$22.50
SM1 Adapter for 20mm Optics	SM1AD20	Thorlabs	$21.50
SM1 Adapter for 18mm Optics	SM1AD18	Thorlabs	$21.50

A **B**

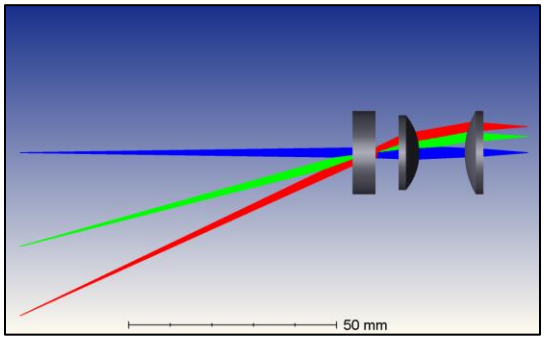

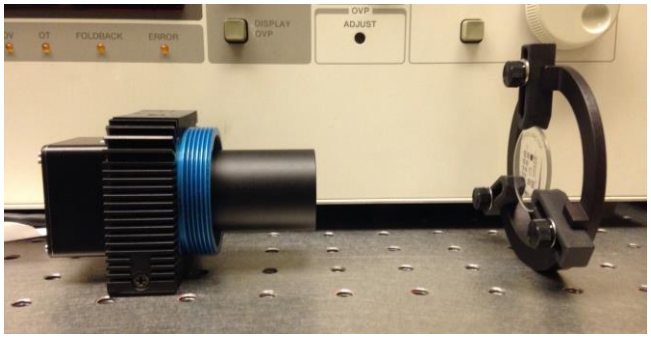

C **D**

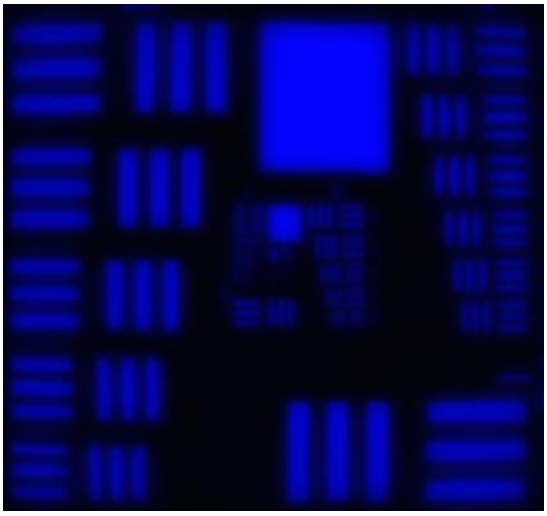

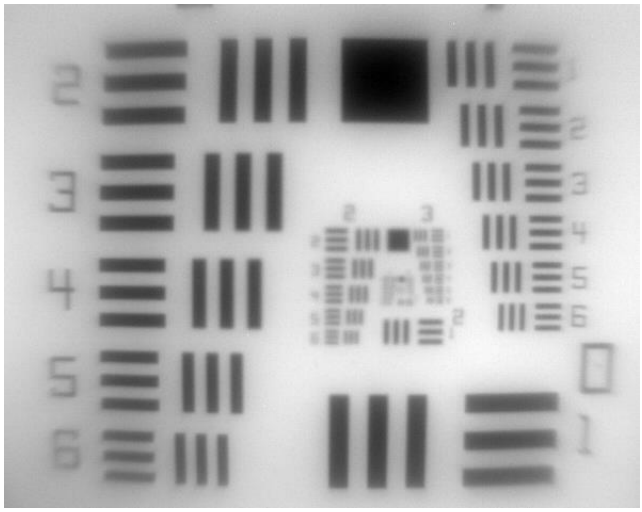

Figure 5-15. Large-scale Objective Prototype. A. Non-sequential ray trace. B. Experimental setup to test the large-scale objective prototype. C. Simulated image of 1951 USAF test target. D. Test image of a 1951 USAF test target captured with the large-scale objective prototype.

5.6 Illumination System Design

5.6.1 Infrared Illumination Source

The infrared illumination source is a custom 4-pin laser diode module operating at 19 discrete wavelengths between 1443-1600 nm (Seminex Corp., Peabody MA). The laser system contains two laser drivers that operate at 4 A and 8 A. Eleven laser units are driven at 8A and eight laser units are driven at 4 A. The output of the system is a 3 millisecond quasi-continuous-wave with a duty cycle of 24%. Each wavelength operation is separately temperature controlled with its own thermoelectric cooling unit to achieve the desired wavelength. The minimum power output per wavelength is 1W. A 0.22 NA multimode optical fiber is attached to the laser module to deliver the light from the laser source to the proximal end of the endoscope.

5.6.2 Optical Fibers

After the infrared light arrives at the proximal end of the endoscope, it is coupled to six 0.5 NA step-index multimode optical fibers using a 1x6 fiber optic tree coupler. The optical fibers guide the infrared light to the distal end of the endoscope, where they are arranged radially and symmetrically in a ring pattern around the optical system. The optical fibers are 425 μm diameter hard polymer cladded optical fibers with a broad spectral range from 400-2200 nm (Model: FP400ERT, ThorLabs, Newton, NJ). Low hydroxyl silica was chosen as the material for the optical fiber core due to its biocompatibility, low attenuation, and peak transmittance at 1550 nm as shown in Figure 5-16. According to the attenuation plot, the transmission is greater than 90% per meter for the entire operating wavelength of the endoscope (Figure 5-16). The operating temperature of the fiber is within the operating temperature of the endoscope (37° C for normal human body temperature). Additional specifications for the optical fibers are listed in Table 5-6.

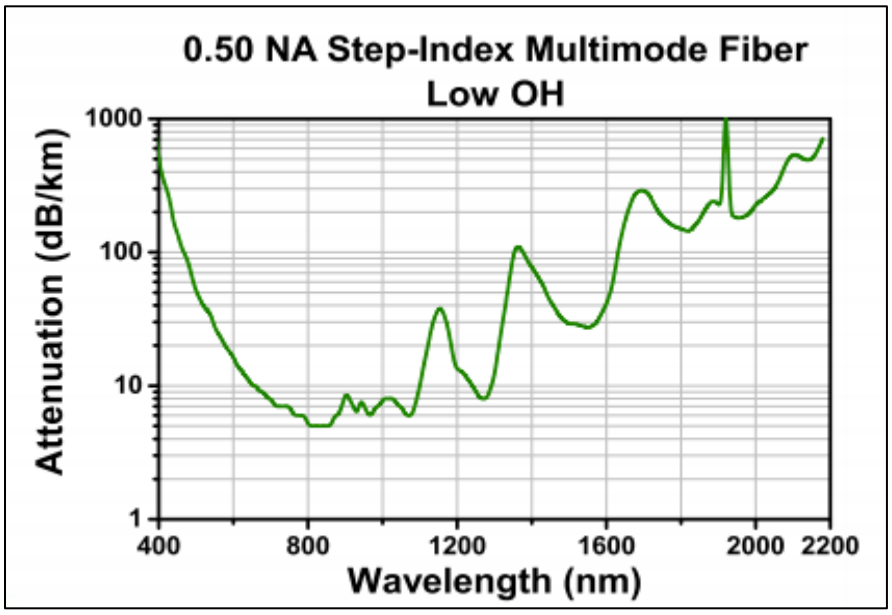

Figure 5-16. Transmittance of Low OH Multimode Fiber as a function of wavelength.

Table 5-6. Low OH Multimode Fiber specifications

Parameter	**Value**
Transmission Region (nm)	400-2200
Core Diameter (um)	400
Cladding Diameter (um)	425
Core Material	Pure Silica
Cladding Material	Hard Polymer
Numerical Aperture NA	0.50
Index of Refraction – Core	1.458
Index of Refraction - Cladding	1.365
Operating Temperature (°C)	-40 to 150

5.7 Non-Sequential Ray Tracing Simulations

5.7.1 System Setup

The illumination profile of the optical fibers was simulated using non-sequential ray tracing software, Advanced Systems Analysis Program (ASAP) (Breault Research Organization, Tucson AZ). To model the laser light source, six 0.425 um diameter Lambertian emitting disks with a half angle of 30 degrees were created and coupled to each optical fiber. The coupling efficiency was maximized since the NA of the fiber and that of the source were equal. The six optical fibers were arranged radially and symmetrically in a ring pattern around the imaging system (Figure 5-17a). The diameters of the optical fibers were 0.425 um, the index of refraction of the silica glass core was 1.458, and the index of refraction of the polymer cladding was 1.365. Fresnel equations were applied at the core and cladding boundaries to calculate the appropriate amounts of reflected and transmitted light. The attenuation of the optical fiber was assumed to be negligible due to the short length of the endoscope and the absence of bending. The wavelength of the system was set to 1550 nm and the power from all sources was normalized to 1.

In addition to the illumination system components, several geometric surfaces were created in the simulation to represent the imaging system, the endoscope body, and the object surface. The geometric surfaces had no effect on the properties of the illumination system and are only used for reference. A 3-mm diameter inner tube, which contains the optical imaging components, is located at the center of the endoscope model to represent the space occupied by the imaging system. The imaging system and optical fibers of the illumination system are enclosed by a 4.3 diameter outer tube, which represents the body of the endoscope. A 30-mm diameter circular detector surface located 20 mm away from the distal end of the endoscope simulated the object location and the working distance of the endoscope (Figure 5-17c).

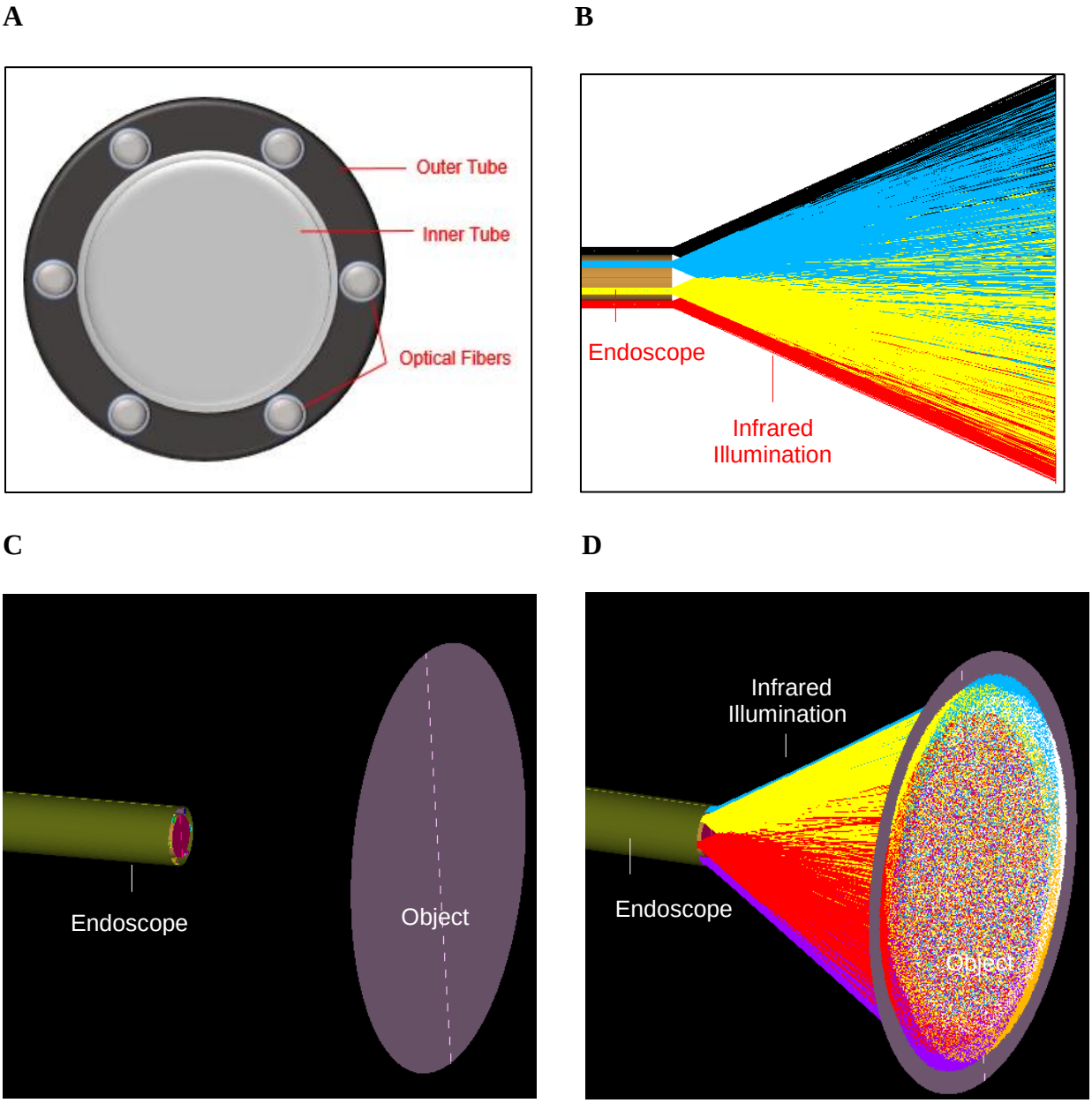

Figure 5-17. 3D Viewer of the illumination system on ASAP. A. Front-face view of the distal end of the endoscope. B. Side view of the illumination system at the distal end of the endoscope showing the emitting profile of the fiber bundle. C. CAD model of the distal end of the endoscope relative to the object surface. D Non-sequential ray trace of the illumination system relative to the object surface.

5.7.2 Results and Discussion

The overall performance of the illumination system was evaluated by analyzing the normalized irradiance distribution at the detector located at the working distance of the imaging system. Because total internal reflection does not change the angle of the rays relative to the optical axis, when light propagates through a straight optical fiber, the NA of the output is equal to the NA of the input. Based on the results of the simulation, the maximum emission angle at the distal end of the endoscope is approximately 30 degrees (Figure 5-17b), which agrees with the theoretical value derived from the NA of the optical fiber. The output of the illumination system at the detector is a spotlight of approximately 26 mm in diameter, which is greater than the diameter of the imaging field of the endoscope (Figure 5-18). Therefore, the lighting from the optical fibers was shown to provide a large area of illumination that sufficiently covers the entire field of view of the imaging system.

A **B**

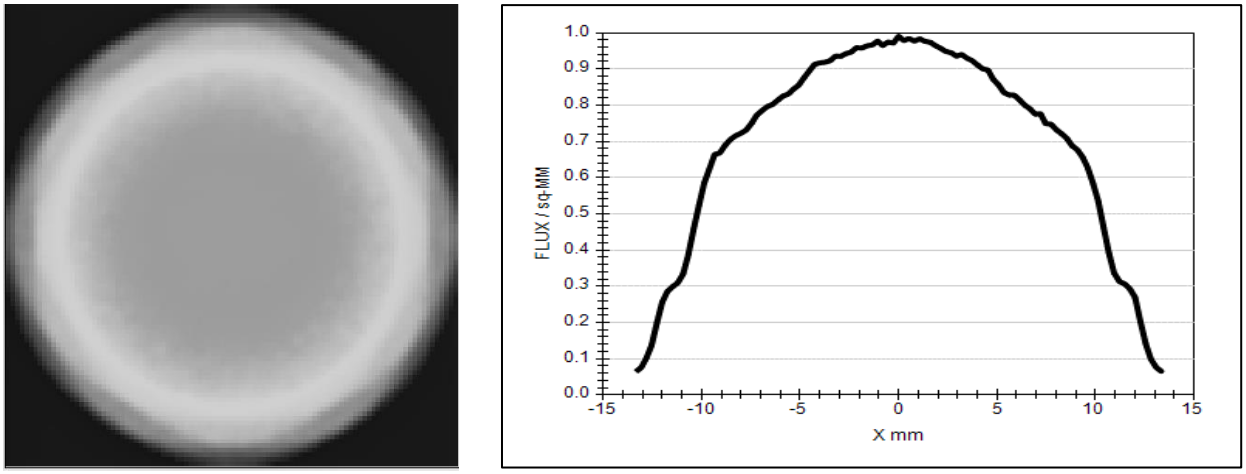

Figure 5-18. Simulated irradiance of the imaging system. A. Simulation of the light at the detector surface 20 mm away from the distal end of the endoscope. B. Normalized irradiance distribution of the endoscope illumination system at the detector.

Another observation of the illumination profile is that the intensity of the light at the outer edge of the field is much less than that of the center of the field. As shown in the normalized irradiance plot in Figure 5-19, the irradiance at 10 mm away from the optical axis is approximately 50% of the irradiance at the center. This is due to the optical path of the higher angle light rays being longer and the frequency of reflections at the boundary between the core and cladding being greater, which results in more losses due to absorption and reflection [36]. The distribution of the light emitted from the multimode optical fiber can be calculated by the following equation:

$$I(\theta) = I_0 e^{-2\left(\frac{\theta}{\alpha}\right)^2} \quad \text{(Eq. 5-4)}$$

where I_0 is the intensity of light at the optical axis, θ is the angle light of formed with the optical axis, and α is the divergence angle of the emitted light.

Equation 5-4 shows that the angular distribution of light is a Gaussian function, which agrees with the general shape of the plot in Figure 5-19. Absorption losses are the result of impurities in the fiber optic glass material such as hydrogen or oxygen molecules or other metal ions, which decrease the divergence angle α in Equation 5-4. This results in the intensity of light to decrease to $1/e^2$ of the axial value at smaller angles as the irradiance is measured across the field. Other sources of losses include bending, fiber defects, and local distortions, which may result in a radiated angle that is smaller than the aperture angle. However, the absence of bending in the fiber in this illumination system design minimizes the amount of losses due the bending.

One simplifying assumption that was made in the non-sequential ray tracing simulation was that the coupling efficiency between the light sources and the optical fibers was maximized. Therefore, the coupling of the lower NA optical fiber from the laser module to the higher NA

optical fiber at the proximal end of the endoscope was not modeled in the simulation. When a lower NA optical fiber is coupled to a higher NA fiber, higher angle modes in the higher NA fiber may not be excited. This is known as an under-filled condition and results in light being concentrated spatially in the center of the fiber. Thus, a smaller output angle would be formed when the fiber illuminates the field of view. However, using a glass-truncated cone in the fiber coupler can minimize the effects of the under-filled condition. When the lower NA optical fiber is being coupled to the higher NA fiber, the larger end of the truncated-cone is coupled to the smaller NA fiber and the smaller end of the cone is coupled to the larger NA fiber. This coupling method increases the excitation angle of the larger NA fiber in the endoscope, thereby increasing the output angle at the distal end of the endoscope.

Several illumination systems were also evaluated in addition to the current optical fiber configuration, but those results are not reported here due to space limitations. One of those systems included a single fiber optic bundle configuration adjacent to the imaging system. Compared to the current optical fiber illumination system, a single fiber bundle illumination design could potentially be more complex and less cost effective by requiring additional optical components. If a single optical fiber or fiber bundle were used without additional optical components, the peak irradiance would be shifted away from the optical axis of the imaging system, due to the asymmetric positioning of the fiber bundle relative to the optical axis. The asymmetric position of the fiber bundle would prevent uniform illumination across the entire field of view and may produce undesirable shadowing effects. Methods to correct the shift include tilting the optical fiber or adding additional optics such as prisms, which would be necessary to shift the peak irradiance back to the center of the viewing field to obtain uniform illumination.

5.8 Summary and Conclusions

The current prototype of this device has light losses in both the illumination system and image relay. Minimizing these losses in the ray-tracing simulations can improve the quality of images in future prototypes. By optimizing the lens design and using custom optical lenses, it is possible to obtain higher resolution trans-blood images. Possible future prototypes may include modifications to the size of the optics to accommodate surgical tools and probes. These tools and probes may be used and imaged in real-time during suturing, excising, and stapling procedures if they are in the imaging field of the endoscope. To increase the field of view, additional lenses may be added to the tip of the endoscope, allowing a larger field to be accepted by the objective lens. Imaging enhancement software can be written to remove background noise and correct distortion during image processing. Additionally, more sensitive imaging sensors in the infrared camera can decrease the minimum amount of light needed to generate a signal for the camera image. With future advancements in optics research, technological improvements in the resolution and sensitivity of imaging sensors as well as other optical components will allow for even smaller rigid endoscopes to be made. The scope of a rigid trans-blood imaging endoscope has potential applications beyond the field of clinical cardiology and may lead to medical procedures that have yet to be developed.

CHAPTER 6:
CONCLUSIONS AND FUTURE WORK

6.1 Summary of Work

Current methods for imaging through blood using visible light results in significant scattering and absorption, which yields poor quality images. However, according to Mie scattering theory, imaging through blood using infrared light is feasible. Intra-cardiac imaging through blood using a fiber-optic infrared endoscope was previously investigated and demonstrated in the literature. However, this thesis successfully demonstrated the feasibility of a rigid trans-blood endoscope with GRIN relay optics for intra-operative imaging inside the heart. Two different imaging systems were designed and optimized, and both were shown to be feasible for trans-blood imaging. Additionally, the results of the simulation of the fiber optic illumination system indicated that sufficient illumination was provided over the entire field of view. Overall, a rigid trans-blood endoscope is much more cost-effective and offers higher resolution images and performance compared to the previously commercially available fiber optic design. After the completion of the mechanical design of the endoscope, future work will include *in vitro* experiments and testing in animal models before clinical studies can begin.

6.2 Future Work and Experiments

6.2.1 Mechanical Design

The mechanical design of the endoscope must be able to perform the following: mount the lenses of the imaging system, house the optical fibers of the illumination system, and connect the lenses of the imaging system to the focal plane array of the IR camera. The endoscope will be made from a 3-mm diameter inner tube placed inside a 4.3 mm diameter outer tube machined from surgical stainless steel. The inner lens tube will be machined to house the lenses of the imaging system, while spacers and retaining rings will be used to maintain the precise separation distances between lenses. The optical fibers of the illumination system will be assembled in between the outer and inner tubes. A custom lens mount will be machined to mount the endoscope to the c-mount on the IR camera

An important mechanical design criterion of the endoscope is that the physical dimensions must be compatible with the patient anatomy. The endoscope is designed to access the right atrium of the patient via the internal jugular vein. Therefore, the average diameter of the right atrium and internal jugular vein should be greater than the outer diameter of the endoscope. The average diameter of the internal jugular vein is 13.4 mm for adults and 5 mm for pediatric patients (0-6 months of age) [41] [42], while the average diameter of the right atrium for an adult and pediatric patient is 45 mm and 37 mm respectively [43]. Additionally, the total length of the endoscope should be greater than the average distance between the internal jugular vein and the left atrium. The average distance between the internal jugular vein and the left atrium is approximately 160 mm for an adult [44]. To meet these size constraints, the total length and diameter of the endoscope outer tube will be approximately 183 mm and 4.3 mm respectively (Figure 6-1).

A **B**

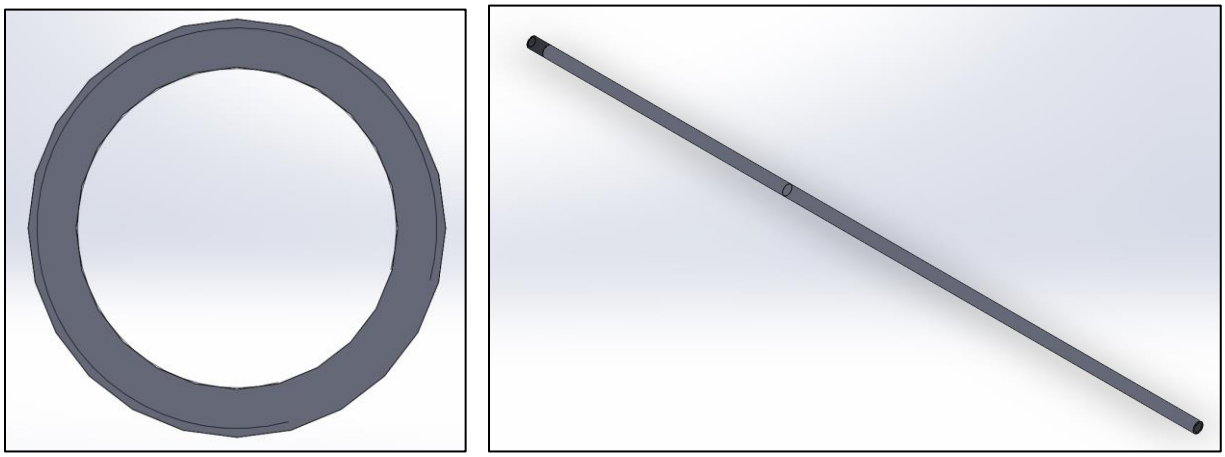

C

Figure 6-1. CAD drawings of endoscope housing. A. Front-face view. B. Isometric view. C. Side-view.

6.2.2 *In vitro* experiments

In vitro experiments designed to obtain images through heparinized blood are planned immediately after completion of both the imaging and illumination systems. A 12.5 x 12.5 mm sample cuvette holder was designed using SolidWorks and machined in the UCLA Engineering Student Machine Shop (Figure 6-1a & b). Infrared light from the illumination system will be directed into a Quartz cuvette containing 3mL heparinized porcine blood (Figure 6-1c). The path length of the cuvette is 1 cm, which approximates the working distance of the endoscope. The completed imaging system will be used to capture trans-blood images of a 1951 USAF test target located at the other end of the cuvette (Figure 6-1d). The data collected from these experiments would be used evaluate the performance of the imaging system. Additionally, the power output

of the illumination system can be adjusted accordingly to provide adequate illumination while minimizing the damage to blood and surrounding tissues.

Difficulties obtaining trans-blood images from *in vitro* experiments are expected due to the use of stored or stationary blood. Previous experiments in the literature encountered difficulty in obtaining images *in vitro* using stored or stationary blood, which would suggest that the technology might have limitations [30]. This is because cellular components in heparinized blood have been shown to induce Rouleaux formation or aggregation, which increases the effective diameter of red blood cells, resulting in a change in the scattering properties of blood. However, this issue can be resolved by performing experiments using *in vitro* models where the blood is flowing continuously with the use of pumps.

6.2.3. *In Vivo* experiments

Besides demonstrating the feasibility of a rigid trans-blood imaging endoscope *in vitro*, the system will require testing in a functioning and beating heart. While the *in vitro* experiments would demonstrate that trans-blood imaging is feasible in a static environment, the beating heart is a highly dynamic environment with living cells and tissues. Therefore, biocompatibility and the effects of convective blood flow on image stability may not be apparent in *in vitro* experiments. *In vivo* experiments are planned in the future on animal models to study these effects. To date, the animal protocol has completed pre-committee review and is pending approval from the UCLA Animal Research Committee. *In vivo* experiments would involve introducing the endoscope and the illumination system through separate channels of a custom endoscope port into the right atrium of sedated Gottingen mini pigs. Insertion of the endoscope via the right internal jugular vein and placement of the endoscope will be guided using

ultrasound. Areas of specific interest to image include heart valves and chordae tendinae. Other intra-operative cardiac imaging modalities such as ultrasound and fluoroscopy will also be used to compare images.

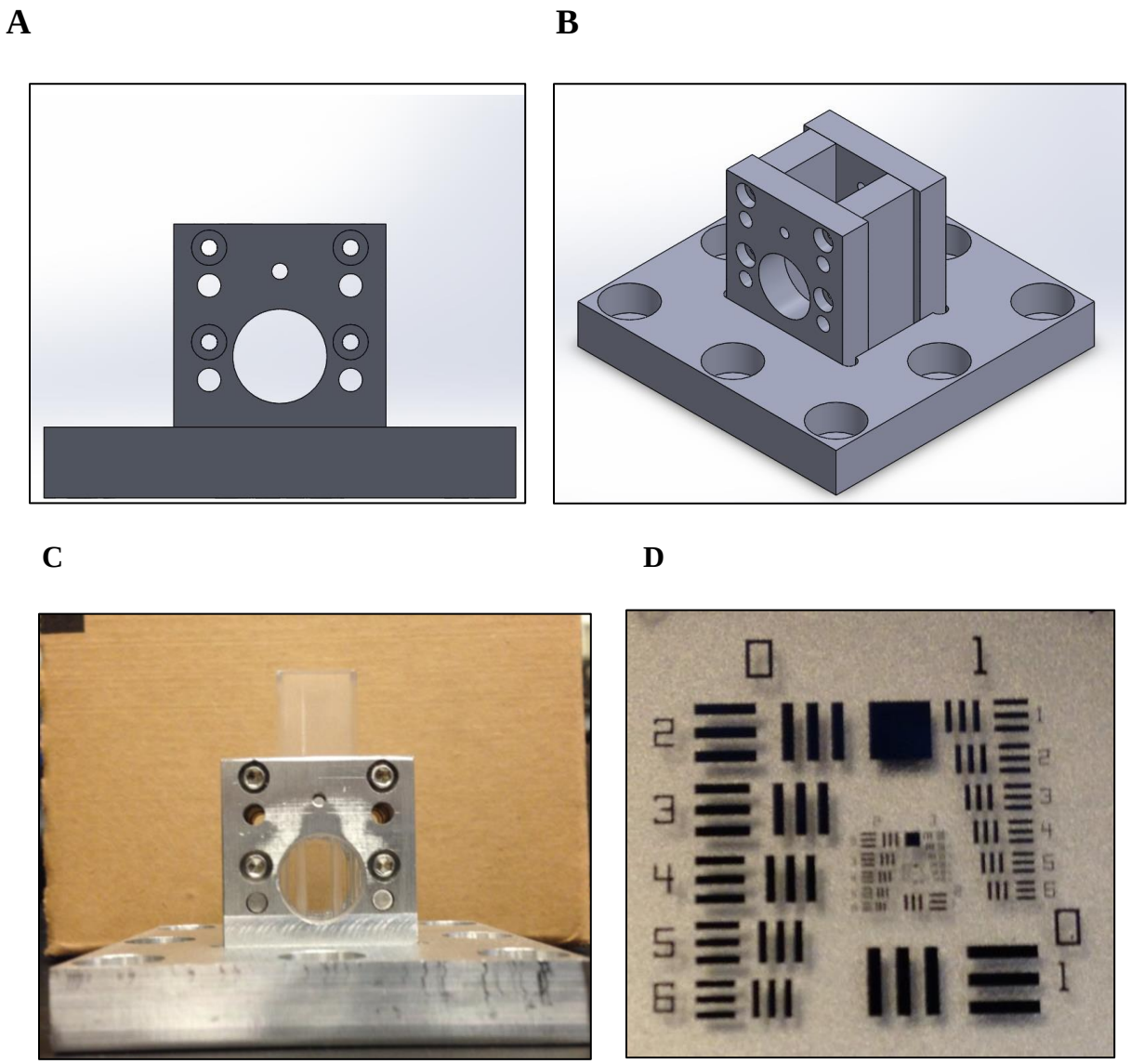

Figure 6-2. Sample cuvette holder to be used in future *in vitro* experiments. A. Front-face view. B. Isometric View. C. Machined cuvette holder holding empty cuvette. D. USAF 1951 Test resolution chart

References

[1] Hall, John E. *Guyton and Hall textbook of medical physiology*. Elsevier Health Sciences, 2015.

[2] Page E, Fozzard HA, Solaro JR: Handbook of Physiology, sec 2: The Cardiovascular System, vol 1: The Heart. New York: Oxford University Press, 2002.

[3] Venes, D. "Taber's cyclopedic medical dictionary Vol 2." (2009).

[4] Hinton, Robert B., and Katherine E. Yutzey. "Heart valve structure and function in development and disease." *Annual review of physiology* 73 (2011): 29.

[5] Klabunde, Richard. *Cardiovascular physiology concepts*. Lippincott Williams & Wilkins, 2011.

[6] Walker, Brian R., and Nicki R. Colledge. *Davidson's principles and practice of medicine*. Elsevier Health Sciences, 2013.

[7] Hoffman JI, Kaplan S: The incidence of congenital heart disease. J Am Coll Cardiol 39:1890, 2002.

[8] Tutar E, Ekici F, Atalay S et-al. The prevalence of bicuspid aortic valve in newborns by echocardiographic screening. Am. Heart J. 2005;150 (3): 513-5.

[9] Brickner, M. Elizabeth, L. David Hillis, and Richard A. Lange. "Congenital heart disease in adults." *New England Journal of Medicine* 342.4 (2000): 256-263

[10] Reimold SC, Rutherford JD: Clinical practice: valvular heart disease in pregnancy. N Engl J Med 349:52, 2003.

[11] Agabegi, Steven S., and Elizabeth D. Agabegi. *Step-up to Medicine*. Vol. 3. Lippincott Williams & Wilkins, 2012.

[12] Mettler Jr, Fred A., et al. "Effective doses in radiology and diagnostic nuclear medicine: a catalog 1." *Radiology* 248.1 (2008): 254-263

[13] Bonow, R. O., et al. "ACC/AHA guidelines for the management of patients with valvular heart disease. Executive summary. A report of the American College of Cardiology/American Heart Association Task Force on Practice Guidelines." *The Journal of heart valve disease* 7.6 (1998): 672

[14] Cavaye, Douglas M., and Rodney A. WHITE. *A Text and Atlas of Arterial Imaging: Modern and Developing Technology*. Chapman & Hall Medical, 1993

[15] Burnett, J. Mark. "RCP et al., Intracardiac Echocardiography 101: The Beginner's Guide to ICE Imaging and Cardiac Structure Recognition." (2007).

[16] Becker, Anton E. "Left atrial isthmus." *Journal of cardiovascular electrophysiology* 15.7 (2004): 809-812.

[17] Ommen, S. R., et al. "Clinical utility of Doppler echocardiography and tissue Doppler imaging in the estimation of left ventricular filling pressures a comparative simultaneous Doppler-catheterization study." *Circulation* 102.15 (2000): 1788-1794

[18] Bartel, Thomas, et al. "Intracardiac echocardiography: a new guiding tool for transcatheter aortic valve replacement." *Journal of the American Society of Echocardiography* 24.9 (2011): 966-97

[19] D. Malacara-Hernández, "Optics for Engineers," in Photomechanics, vol. 77, P. K. Rastogi, Ed. Berlin, Heidelberg: Springer Berlin Heidelberg, pp. 1–32.

[20] V. V. Tuchin and Society of Photo-optical Instrumentation Engineers, Tissue Optics:Light Scattering Methods and Instruments for Medical Diagnosis, 2nd ed. Bellingham, Wash: SPIE/International Society for Optical Engineering, 2007.

[21] Amundson, David C., and H. John Hanlin. "Infrared endoscopic imaging in a liquid with suspended particles: method and apparatus." U.S. Patent No. 6,178,346.23 Jan. 2001.

[22] S. L. Jacques, "Introduction to Biomedical Optics," Introduction to Biomedical Optics, Jan-1998.

[23] J. Mobley and T. Vo-Dinh, "Optical Properties of Tissue," in Biomedical Photonics Handbook, T. Vo-Dinh, Ed. CRC Press, 2003.

[24] C. F. Bohren and D. R. Huffman, "Particles Small Compared with the Wavelength," in Absorption and Scattering of Light by Small Particles, Wiley-VCH Verlag GmbH, 2007.

[25] C. F. Bohren and D. R. Huffman, "Angular Dependence of Scattering," in Absorption and Scattering of Light by Small Particles, Wiley-VCH Verlag GmbH, 2007.

[26] L. Grossweiner, J. Grossweiner, and B. H. Gerald Rogers, "The Science of Phototherapy: An Introduction," Springer Netherlands, 2005, pp. 9–55.

[27] Hulst, Hendrik Christoffel, and H. C. Van De Hulst. Light scattering by small particles. Courier Corporation, 1957.

[28] Grundfest WS, Litvack F, Lee ME, "High-resolution intraoperative angioscopy of peripheral and coronary arteries in man". Surg Forum 35:423-425, 1984

[29] Grundfest WS, Litvack F, Sherman T, et al: Delineation of peripheral and coronary detail by intraoperative angioscopy. Ann Surg 202:394-400, 1985

[30] Grundfest, Warren S., et al. "Real-time percutaneous optical imaging of anatomical structures in the heart through blood using a catheter-based infrared imaging system." *Seminars in thoracic and cardiovascular surgery*. Vol. 19. No. 4. WB Saunders, 2008

[31] Friebel, Moritz, et al. "Optical properties of circulating human blood in the wavelength range 400–2500 nm." *Journal of biomedical optics* 4.1 (1999): 36-46.

[32] Steinke, John M., and A. P. Shepherd. "Comparison of Mie theory and the light scattering of red blood cells." *Applied optics* 27.19 (1988): 4027-4033.

[33] Nazarian, Saman, et al. "Direct visualization of coronary sinus ostium and branches with a flexible steerable fiberoptic infrared endoscope." *Heart Rhythm* 2.8 2005: 844-848.

[34]Knight, Bradley P., et al. "Direct imaging of transvenous radiofrequency cardiac ablation using a steerable fiberoptic infrared endoscope." *Heart Rhythm* 2.10 2005: 1116-1121.

[35] http://www.accessdata.fda.gov/cdrh_docs/pdf6/K062340.pdf. Accessed Feb 21 2016.

[36] Rongguang. *Optical design for biomedical imaging*. Spie Press, 2010.

[37] H. H. Hopkins, “Optical principles of the endoscope,” in Endoscopy, G. Berci, Ed., pp. 3–26, Appleton-Century-Crofts, New York (1976).

[38] Endoscopy, G. Berci, Ed., pp. 3–26, Appleton-Century-Crofts, New York (1976).

[39] http://www.edmundoptics.com/resources/application-notes/optics/anti-reflection-coatings/

[40] Jenny, Reinhard. "Fundamentals of fiber optics: An introduction for beginners." Volpi Manufacturing USA Co., Inc. Auburn, NY (2000): 1-22. APA

[41] Furukawa, Satoshi, et al. "The diameter of the internal jugular vein studied by autopsy." *Rom J Leg Med* 2 (2010): 125-8.

[42] Sayin, Murat M., et al. "Internal jugular vein diameter in pediatric patients: are the J- shaped guidewire diameters bigger than internal jugular vein? An evaluation with ultrasound." *Pediatric Anesthesia* 18.8 (2008): 745-751

[43] Kutty, Shelby, et al. "Systemic venous diameters, collapsibility indices, and right atrial measurements in normal pediatric subjects." Journal of the American Society of Echocardiography 27.2 (2014): 155-162.

[44] Andrews, Robert T., Dawn A. Bova, and Anthony C. Venbrux. "How much guidewire is too much? Direct measurement of the distance from subclavian and internal jugular vein access sites to the superior vena cava-atrial junction during central venous catheter placement." *Critical care medicine* 28.1 (2000): 138-142.